RADIAL AGE AND METAL ABUNDANCE GRADIENTS IN THE STELLAR CONTENT OF M32

James A. Rose

Department of Physics and Astronomy, University of North Carolina, Chapel Hill, NC 27599

Electronic mail: jim@physics.unc.edu

Nobuo Arimoto

National Astronomical Observatory of Japan, Mitaka, Tokyo, Japan

Electronic mail: arimoto@optik.mtk.nao.ac.jp

Nelson Caldwell

F.L. Whipple Observatory, Smithsonian Institution, Box 97, Amado AZ 85645

Electronic mail: caldwell@flwo99.sao.arizona.edu

Ricardo P. Schiavon

Department of Astronomy, University of Virginia, P.O. Box 3818, Charlottesville, VA 22903-0818

Electronic mail: ripisc@virginia.edu

Alexandre Vazdekis

Instituto de Astrofisica de Canarias, La Laguna, Tenerife, Spain

Electronic mail: vazdekis@ll.iac.es

Yoshihiko Yamada

National Astronomical Observatory of Japan, Mitaka, Tokyo, Japan

Electronic mail: yyamada@optik.mtk.nao.ac.jp

ABSTRACT

We present long-slit spectroscopy of the elliptical galaxy M32, obtained with the 8-m Subaru telescope at Mauna Kea, the 1.5-m Tillinghast telescope at the F. L. Whipple Observatory, and the 4-m Mayall telescope at the Kitt Peak National Observatory. The spectra cover the Lick index red spectral region as well as higher order Balmer lines in the blue. Spectra have been taken with the slit off-set from the nucleus to avoid scattered light contamination from the bright nucleus of M32. An analysis of numerous

absorption features, particularly involving the Hγ and Hβ Balmer lines, reveals that systematic radial trends are evident in the integrated spectrum of M32. Population synthesis models indicate a radial change in both the age and chemical composition of the light-weighted mean stellar population in M32, from the nucleus out to 33″, i.e., approximately 1.0 effective radius, R_e. Specifically, the light-weighted mean stellar population at 1 R_e is older, by ∼3 Gyr, and more metal-poor, by ∼−0.25 dex in [Fe/H], than the central value of ∼4 Gyr and [Fe/H]∼0.0. We show that this apparent population trend cannot be attributed to a varying contribution from either hot stars or emission line contamination. The increase in age and decrease in metal-abundance with radius are sufficiently well-matched to explain the flat radial color profiles previously observed in M32. In addition, the ratio of Mg to Fe abundance, [Mg/Fe], increases from ∼−0.25 in the nucleus to ∼−0.08 at 1 R_e. Finally, we find spuriously pronounced line strength gradients in the Mayall data that are an artifact of scattered light from the bright nucleus. Scattered light issues may explain the lack of consistency among previously published studies of radial line strength gradients in M32.

Subject headings: galaxies: evolution — galaxies: elliptical and lenticular, cD

1. Introduction

Due to its proximity and high central surface brightness, the elliptical galaxy M32 has often served as a unique testing ground for evaluating the modelling of the integrated light of galaxies and thereby disentangling key aspects of the star formation and chemical enrichment histories of galaxies. In fact, M32 is still the only elliptical galaxy for which it is possible to obtain both integrated light spectroscopy and an extensive CMD of the giant branch (using *HST*) at the same location in the galaxy. Thus it presents a powerful testing ground of the reality of integrated light analyses of galaxies. Unfortunately, M32 represents a rather special case elliptical, given its status as a low-mass satellite galaxy to M31, its probable tidal truncation as a result of close proximity to M31 (e.g., Bekki et al. 2001; Choi, Guhathakurta, & Johnston 2002), and its rare (cE) morphology. Hence it is encouraging that resolved star studies of the upper giant branch of the more normal and massive elliptical galaxy NGC 3379 have been pursued recently by Gregg et al. (2004). Given its proximity, however, M32 remains the ideal galaxy for testing inferences from integrated light spectroscopy and broadband colors against resolved star observations.

In the context of constraining galaxy formation scenarios, determining radial population gradients in elliptical galaxies can play a key role. Specifically, the predicted gradient in metallicity is substantially flatter in the case of a hierarchical structure formation picture than it is for a monolithic collapse scenario (e.g., Kobayashi & Arimoto 1999). Due to the high surface brightness of M32, one can readily study the integrated spectrum out to a radial distance of 30″, or 1 effective radius, R_e. However, previous studies of radial color and line strength gradients in M32 have led

to strikingly discordant results. On the one hand, Peletier (1993) finds that all colors, as well as the CO index, remain constant with radius, and concludes that no age gradient exists in M32. Moreover, in *HST* images of the central regions of M32, Lauer et al. (1998), find no gradient in V−I color, and only a very small blueing in U−V with increasing radius. In addition, *some* individual spectral features exhibit no signs of a radial gradient in line strength. Specifically, both the Mg_2 index (Davidge 1991) and Mg b index (González 1993; Fisher, Franx, & Illingworth 1995) appear to be constant with radius, as is Fe5015 (Fisher, Franx, & Illingworth 1995). There is, however, considerable uncertainty concerning the flatness of the Mg_2 radial profile, since Hardy et al. (1994) report a decline in this index with radius out to a distance of 60″, or approximately 2 effective radii, R_e.

On the other hand, Cohen (1979), Davidge, de Robertis, & Yee (1990), and Davidge (1991) have found radial line strength gradients in a number of spectral features, as have Fisher, Franx, & Illingworth (1995) for the λ4668 feature. The long-slit data of González (1993), as reported in Fisher, Franx, & Illingworth (1995; cf., their Fig. 9), indicates a decrease in Hβ strength with increasing radius. However, Hardy et al. (1994) find a flat profile in Hβ out to 60″ in radius. In addition, neither Fisher, Franx, & Illingworth (1995) nor del Burgo et al. (2001) find a radial trend in Hβ, although the latter two studies reach only to 20″ and 15″ respectively. In addition, Ohl et al. (1998) have found a strong far-UV (FUV) (1500Å) color gradient in M32, such that the FUV−B color becomes bluer at increasing radial distance, which is the reverse of the other early-type galaxies that they studied. Ohl et al. speculate that the FUV gradient in M32 could be due to increasing age with radius, but also mention the possibility of a varying helium abundance. Such a UV color gradient, however, has *not* been found in recent GALEX observations (Gil de Paz et al. 2003). As summarized by Davidge (1991), although there is considerable disagreement between investigators about the reality of line strength gradients in many (if not most) features, a consistent interpretation of both line strength and color behavior can be found if there is a radial gradient in M32 in both age and chemical composition, in the sense that the age increases with radial distance while the metallicity decreases.

The most comprehensive study to date of the resolved stellar population of M32 has been carried out by Grillmair et al. (1996), who resolved individual stars down to slightly below the level of the horizontal branch (HB) with *HST* WFPC2. The observations cover an area at a radius of $\sim$1−2′($\sim$2−4 R_e), with the PC chip field centered at 58″ from the nucleus. Grillmair et al. (1996) find a large spread in metallicity among the giant branch stars, although the spread is less than that predicted in the simple closed box model of Searle & Sargent (1972). The peak in the metallicity distribution appears to be near solar, with a metal-weak tail extending to below [Fe/H]=−1. A mean iron abundance of [Fe/H]=−0.25 is derived for an assumed mean age of 8.5 Gyr, which is consistent with the results inferred from modeling of the integrated light indices of González (1993), extrapolated out to the radius of the PC chip. In contrast, integrated light studies of the nucleus of M32 typically indicate a mean age of $\sim$3−7 Gyr and [Fe/H]$\sim$0.0 (e.g., Jones & Worthey 1995; Vazdekis & Arimoto 1999; Trager et al. 2000; Worthey 2004; Caldwell, Rose , & Concannon 2003;

Schiavon, Caldwell, & Rose 2004). A number of studies have been made in the past of the AGB-tip stars in M32, first from ground-based optical and IR imaging in good seeing (Freedman 1989, 1992; Davidge & Nieto 1992; Elston & Silva 1992), and recently from adaptive optics IR imaging from CFHT and Gemini-North by Davidge (2000) and Davidge et al. (2000). The earlier work found AGB-tip stars luminous enough to indicate the presence of a substantial ($\sim$10$-$15%) intermediate age population in M32, while the adaptive optics studies have now pushed the same conclusion to a radial distance of only 2″. As reported by Davidge et al. (2000), the implication of this recent work is that an intermediate age population is uniformly spread over at least the central 2′ of M32, with no evidence for a radial age gradient. On the other hand, *HST* near-UV imaging of M32 by Brown et al. (1998) reveals that the resolved UV-bright stars are more centrally concentrated than the underlying unresolved UV sources, which indicates some type of radial population gradient.

It is clearly important to resolve the apparent discrepancy that exists between color-based measurements and those based on individual absorption features (as well as the implications of the resolved star imaging), since many conclusions about the behavior of early-type galaxies are based on colors alone (given that high S/N ratio long-slit spectroscopy is difficult to obtain for distant galaxies). If radial population gradients in age and metallicity exist in M32, in approximate proportions so as to cancel out the primary color effects that each alone causes, as the line strength measurements suggest, then the interpretation of color gradients in more distant galaxies could be problematic. With that issue in mind, we present integrated light spectroscopy for M32 out to a radial distance of $\sim$30″ ($\sim$1 R_e). While not far enough to overlap with the *HST* CMD study of Grillmair et al. (1996), a sufficient radial distance from the nucleus is achieved to establish the existence of a significant radial population gradient in M32, and thereby to link the CMD study with the numerous integrated light analyses of the nucleus. The emphasis of our study is on decoupling age and metallicity effects using measurements of several Balmer lines.

Here we combine long-slit spectroscopy from three telescope, spectrograph, and detector combinations to evaluate the radial behavior of stellar populations in M32. The plan of the paper is as follows. In §2 we describe the three spectroscopic datasets, while the spectral indicators and populations synthesis models employed are presented in §3. In §4 we first establish from two of the datasets that there is a small but significant radial change in the light-weighted mean age and metallicity of M32 from the nucleus out to a radial distance of 30″. Then we demonstrate how scattered light from the bright nucleus of M32 leads to an artificially strong apparent population gradient in the third dataset. Some implications of the observed age/metallicity gradient are briefly considered in §5.

2. Observational Data

2.1. Subaru + FOCAS

Long-slit spectra have been obtained of the elliptical galaxy M32 with the 8-m Subaru telescope at Mauna Kea with the FOCAS imaging spectrograph (Kashikawa et al. 2000). All spectra were obtained on the night of January 27, 2003. The spectra are imaged onto a 2K X 4K MIT CCD with 15 μ pixels, and binned by a factor of two in the spatial direction, to achieve 0.2″/pixel. A slit width of 0.6″ was used, and the spectra cover the wavelength region 3960 − 5560 Å at a dispersion of 0.655 Å/pixel, and a spectral resolution of 93 km s^{-1} , or ∼3.1 Å FWHM at 4200 Å.. The slit was oriented at a position angle of 80° E of N for all observations, which is only 10° from the minor axis, at ∼70° E of N (Tonry 1984; Kent 1987 both report the PA of the major axis of M32 to be ∼−20° E of N).

The following exposures have been acquired. First, two 300 second exposures were made with the slit centered on the nucleus of M32. Then, a series of three 900 second exposures were made with the slit offset by 10″ from the nucleus, to moderate scattered light from the nucleus for analysis of the fainter outer region of M32. In addition, a 900 second sky exposure was taken at a position offset by 6′ East from the nucleus of M32. Note that the precise locations and PA of the slit for both the M32 and sky exposures is critical here, since we found from both these, and earlier, observations that the slit can intersect one or more planetary nebulae (PN) in M32 and/or a faint HII region in the outer disk of M31. We indeed find that our slit position centered on the nucleus of M32 intersects two PN that are ∼8 and 9.5″ along the slit to the NE, specifically, PN #24 and #25 in Table 6 of Ciardullo et al. (1989).

Data reduction was carried out mainly with IRAF packages in the standard way for long slit data; i.e. overscan correction, bias subtraction, flat fielding, λ calibration, sky subtraction and flux calibration. Cosmic rays were removed and interpolated by using the "cleanest" task in the REDUCEME package (Cardiel et al. 1998). We initially ran automatic finding with the following parameters: SIGTHRESHOLD=6.0 in Searching Square=15. We took care to avoid misidentification of CRs around the peak of flux in the spatial direction. Then we checked by eye in three-dimensional surface plots of flux versus position on the CCD frame and edited out CRs found that way. Since CRs can strongly affect the narrowly defined H$\gamma_{\sigma<130}$ measurement, we checked whether CRs exist around the Hγ feature. Fortunately we found no CR within the passbands of the Hγ_σ index.

2.2. Mt. Hopkins 1.5-m + FAST Spectrograph

Long-slit spectra of M32 have also been obtained with the FAST spectrograph (Fabricant et al. 1998) on the 1.5m Tillinghast telescope of the Whipple Observatory, during the night of 27 December 2002. A 600 gpm grating was used with a 3″ slit, which gave a spectral coverage of from

3600 to 5500 Å, at a resolution of 3.1 Å FWHM, and a dispersion of 0.75 Å/pixel on the Loral 3K X 1K CCD. The pixel scale along the slit is 0.57″ per 15μmm pixel; however, the data were binned by 4 pixels along the slit, to reduce the effective read noise in the outer low surface brightness regions of M32. The detector has a read noise of 8.6 e^- and a gain of 1.2 e^-/ADU. A 300 second exposure was taken with the slit centered on the nucleus of M32, at a PA of −20 E of N, i.e., with the slit aligned on the major axis of the galaxy. Then the telescope was moved sufficiently in Right Ascension (RA) so as to move the slit 5″ off the center of M32, and a 900 second exposure was taken. Next, two 900 second exposures were taken with the slit offset by 15″ from the center of M32, again with the repositioning done in RA only. These were sandwiched around a 900 second sky exposure, with the slit offset by 10′ due South of the center of M32. Finally, a series of seven 900 second exposures were taken with the slit offset by 30″ from the center of M32. Again the offset was made in RA, specifically, 2.9 seconds, which results in the slit being displaced by 30″ from the center of M32. Three more sky exposures and four arc lamp exposures were interspersed with these exposures, to provide reliable background subtraction and wavelength calibration. Two of the sky exposures were offset by 15′ due South, while the third was offset by only 10′. Given the major axis orientation of the Tillinghast/FAST slit and the near-minor axis orientation of the Subaru slit, we have sampled both principal axes of M32.

In additon to the above observations, we make use of a series of eight 4-minute exposures on the nucleus of M32 taken on 28 December 2000 with the same instrument configuration as above. The sole difference is that binning along the slit direction was 3 pixels instead of 4 pixels per bin. The total 32 minutes integration provides superior S/N compared to the 5-minute nuclear exposure on 27 December 2002, and the splitting of the integration into eight separate exposures provides added information on errors in the spectral indices.

The Tillinghast/FAST spectra were processed as follows. After bias-removal and flat-fielding, the next step was cosmic ray (CR) removal. For the 15″ and 30″ offset spectra, the procedure is as follows. A difference frame was created between two individual exposures, a and b, with the difference frame given by a−b. In this difference frame, all pixels with counts below −100 were flagged, and replaced with a 0, while all other pixels were set equal to 1. Thus we produce a mask frame with CRs flagged as zeros. Then we ran a program that extends each of the masked pixels by 1 pixel in each direction, to fully mask the wings of CRs. Using this revised mask file, the IRAF *fixpix* routine was run on frame b, to interpolate over the pixels contaminated by CRs. This produced a CR-cleaned version of frame b. To clean frame a, a b−a difference frame was created, and then the same procedure employed. Using this technique, all frames were cleaned of CRs, except for the single short exposure centered on the nucleus of M32, and the 5″ offset exposure. The same procedure was followed to clean the sky frames of CRs.

The next step was to carry out sky subtraction. We found that the arc lamp exposures did not show zero point shifts greater than 0.3 pixels over the course of the M32 observations. Consequently, we felt safe in directly subtracting the nearest sky exposure in UT to a given M32 exposure, which simplifies matters. We then extracted one-dimensional spectra from the two-dimensional sky-

subtracted, CR-cleaned data frames using the IRAF *apall* task. An aperture is defined, a trace is made of the variation in the slit position of the aperture as a function of the dispersion direction, and then the one-dimensional extraction is made based on the trace. Wavelength calibration was supplied by the nearest (in time) arc exposures.

2.3. KPNO 4-m + R-C Spectrograph

Long-slit spectra of M32 were acquired with the Kitt Peak National Observatory (KPNO) 4-m Mayall telescope by Dr. Lewis Jones, as part of his PhD thesis (cf., Jones 1999), on the nights of June 18-20, 1996. The standard R-C spectrograph was used along with a 632 grooves/mm grating KPC-22B, in second order, producing a dispersion of 0.7 Å/pixel and a resolution of 1.8 Å FWHM on the TK2B 2048^2 CCD detector. The wavelength range covered is 3300 Å − 4770 Å. The detector read noise and gain are 4 e^- and 2 e^-/ADU respectively. The full 5´ slit is covered at a scale of 0.69″/pixel; the slit width was 300 μm, or 2″. Due to the late rising of M32, and the desire to observe it at a minimum air mass, the following strategy was used. On each of the three nights of observation, two 1800 second exposures were taken of M32 at the end of the night, preceded by an 1800 second sky exposure. The sky exposure was taken at a Right Ascension that matched the mean airmass of the M32 observations. However, on the first two nights the last M32 exposure extended far enough into the dawn twilight that the background level was substantially elevated; the M32 exposures were taken earlier on the third night, and did not suffer from this problem. We consequently have not used the last M32 exposures on the first and second nights. Thus a total of 2 useful hours of integration on M32 was obtained through 4 individual exposures, and 1.5 hours of sky observation in three exposures. On each night the slit was rotated to the parallactic angle corresponding to the middle of the M32 observations. The positon angle was at 102°, 100°, and 155°, respectively, for the first, second, and third nights. The position angle for the third night is, coincidentally, within a few degrees of the major axis of M32.

Analysis of the above spectra was carried out in the NOAO IRAF software package. After initial trimming, bias-removal, and flat-fielding, the next step was to clean the numerous CRs from the individual sky exposures. This was done in a two-step process. First, the IRAF routine 'cosmicrays' was run, with the following parameters: Threshold= 10.0, fluxratio= 5.00, window=7, npasses=5. This approach removed a majority of the CRs, but still left an unacceptable number in the images. Further lowering of the threshold for CR removal led to removal of high points which are not CRs. Instead, as a second step, the 'median' routine was run, using a 1 x 10 median filter, with the large binning factor oriented parallel to the slit. This step is successful at removing the remaining CRs, except for a few pathological cases which are extended right along the slit direction. The CR-cleaned sky exposures were then directly subtracted from the two M32 exposures from the particular night.

The next step involved removing the remaining CRs from the four individual sky-subtracted M32 exposures. In addition, the data frames needed to be transformed into a coordinate system

in which the slit axis and dispersion axis are orthogonal and oriented along columns and rows. The CRs were cleaned from the sky-subtracted M32 frames using the same technique as described earlier for the FAST spectrograph data. That is, CRs were identified and eliminated from difference images between two exposures. A problem with this procedure is that the counts in the few central rows of the M32 spectra are very high, and do not reproduce well from one exposure to another. Thus many pixels in the central few rows are flagged. To avoid losing all information in the cenral few rows, all of the flagged pixels were subsequently reset to avoid interpolation. As a result, there is the possibility of badly positioned CRs to produce contamination in the inner spectral indices. We did, in fact, detect an instance of such a contaminated spectral index, and recalculated it without the frame which contains the CR hit. Note that we could use the second M32 exposures on the first and second nights for the CR-cleaning purpose, since their backgrounds were only mildly elevated.

Following CR-removal, the four sky-subtracted M32 frames were transformed into a coordinate system in which the slit axis and dispersion axis are orthogonal and oriented directly along columns and rows. The transformation was carried out using the 'fitcoords' routine in IRAF. Then all four frames were averaged into a sky-subtracted wavelength-calibrated frame. Note that this composite M32 long-slit spectrum consists of two exposures at PA=101°and two at PA=155°. Hence the final long-slit spectrum represents a crude azimuthal average of the spectral behavior of M32. From this final averaged M32 frame spectra were extracted at various slit positions, and flux-calibrated using the flux-calibrated spectrum of the nuclear region of M32 from L. Jones's (1999) PhD thesis.

2.4. Extraction of Spectra

One-dimensional spectra were extracted from the two-dimensional data frames using the IRAF 'aptrace' routine to trace the deviation of the M32 spectra from an idealized spectrum oriented strictly along the CCD rows. In performing the extraction (in the 'apall' routine) we used unweighted extraction (as opposed to variance-weighted), since all CRs had been identified and removed by this point. To determine the light-weighted mean radius of each extracted spectrum, we numerically integrated a radius-weighted de Vaucouleurs $r^{1/4}$ surface brightness profile (de Vaucouleurs 1948) over the extracted length and width of the slit. Following Kent (1987) we assumed a mean ellipticity of 0.17 for M32, and effective radii along the major and minor axes of 35″ and 29″ respectively. Given that the Tillinghast/FAST data were taken with the slit aligned parallel to the major axis of M32, the extractions out to a light-weighted radius of ∼39″ correspond to ∼1.3 R_e along the minor axis. The Subaru slit was positioned very close to the minor axis, and the data samples out to 30″, or 0.9 R_e, along the major axis. A journal of observations, specifying the PAs and locations of the various extractions, is given in Table 1.

2.5. Spectral Resolution

To make a consistent set of measurements of the spectral indicators described in §2.5, it is necessary to carefully match the spectral resolution at all positions along the M32 slit, and to determine the radial velocity at each extracted slit position. Resolution variations along the slit can be due either to variation in the internal velocity dispersion from the center outwards in the galaxy or to variations in the spectrograph image quality. While velocity broadening produces an effective resolution change that is contant in $\delta\lambda/\lambda$, spectrograph image quality may vary in a complex manner both along the slit and along the dispersion axis. In what follows, we have assumed that velocity broadening provides the dominant contribution to variations in spectral resolution along the slit.

The degree of velocity broadening for the M32 spectra extracted at various slit positions was determined by cross-correlation with a template spectrum, using the IRAF 'fxcor' task in the 'rv' package. The template is a model spectrum for a 3.55 Gyr solar abundance population from Vazdekis (1999 and available at the URL http://www.iac.es/galeria/vazdekis/vazdekis_models.html). This model spectrum is created from a composite of various stellar spectra in the Jones Coudé Feed Spectral Library, which is available in the NOAO ftp archive (see below in §2.6). The resolution of the stellar spectra, and thus of our model template, is 1.8 Å FWHM. This is different from the 3.1 Å resolution typical of our M32 observations. The fxcor task returns a measure of the FWHM of the cross-correlation peak. To calibrate this parameter, the template spectrum was Gaussian-smoothed by varying σ's and cross-correlated against the original unsmoothed spectrum. The restricted wavelength region of $\lambda\lambda 4000 - 4400$ Å was used, thereby avoiding the Ca II H and K lines. A fit was made to the width parameter versus smoothing σ, in all cases by making a 9-point Gaussian fit to the cross-correlation peak. From a cubic fit to peak width versus σ, a correspondence between the two quantities was established. Using this calibration procedure, all of the extracted spectra of M32 at different locations along the slit were smoothed to the same final spectral resolution. Specifically, all extracted spectra were smoothed to a final Gaussian σ of 130 km s^{-1} , which is in quadrature with the original 1.8 Å FWHM of the template spectrum. Thus the final spectral resolution is equivalent to 4.75 Å at ∼4300 Å.

2.6. Other Observational Data

In addition to the M32 long-slit spectra described above, we use two other sources of data. First, we use an integrated spectrum of the metal-rich Galactic globular cluster 47 Tuc obtained by A. Leonardi and J. Rose with the CTIO 1.5-m telescope in November 1995. An integrated spectrum of the nucleus of M32 was also acquired with the same equipment on the same night, as M32 transited the meridian, with the slit rotated to the parallactic N-S position angle. The characteristics of these spectra, which have a resolution of 3.1 Å FWHM, are described in Leonardi & Rose (2003). Hence a direct comparison is made between M32 and 47 Tuc with the identical

instrument setup, and can thus be tied in to the long-slit M32 data.

Second, we make use of two extensive libraries of stellar spectra obtained with the coudé feed telescope at KPNO. The first library, of 684 stellar spectra, is publicly available at an NOAO FTP site (ftp://ftp.noao.edu/catalogs/coudelib/). The characteristics of the spectra are decribed in Jones (1999) and in the readme file at the website. In brief, the spectra were acquired at 1.8 Å resolution (FWHM), and cover two wavelength intervals, 3820 − 4500 Å and 4780 − 5460 Å. We hereafter refer to this spectral database as the Jones Coudé Feed Spectral Library (JCFSL).

The JCFSL spectra, as well as the M32 spectra and the 47 Tuc integrated spectrum, have been smoothed to the lowest spectral resolution of 3.1 Å FWHM set by the CTIO 1.5-m 47 Tuc data. In the case of the JCFSL, for which resolution differences are due to spectrograph resolution rather than velocity broadening, a gaussian smoothing by a σ of 1.75 pixels in linear wavelength is necesary to attain the resolution of the 47 Tuc integrated spectrum.

The second spectral library, which became available while work for this paper was in progress, is the more extensive Indo-US Library of Coudé Feed Stellar Spectra (hereafter, IUCFSL), which includes 1273, covered at a spectral resolution of ∼1.2 Å FWHM. For most stars the entire region 3460 − 9464 Å is covered. The characteristics of this library, which is also publicly available at an NOAO website (http://www.noao.edu/cflib/), are discussed in Valdes et al. (2004). For these spectra, a correspondingly higher level of smoothing is required to attain the overall resolution of our M32 data.

Finally, to obtain a well-defined zero-point velocity determination, the radial velocity for each of the extracted M32 spectra, and the 47 Tuc spectrum, was determined using as template a population model spectrum based on a weighted composite of JCFSL stars. The method of producing the model spectrum, which has an age of 4 Gyr and solar chemical composition, is discussed in §3.2.

3. Spectral Indices and Population Models

3.1. Spectral Indices

In this section we characterize the different types of spectral indices used in our study. Since these spectral indicators are all discussed extensively elsewhere in the literature, we simply give brief summaries of their principal characteristics and refer the reader to other sources for a more extensive description.

There are a number of possible ways to isolate and measure an individual spectral feature. Here we rely on three different methods, which each have particular advantages depending on the degree of line crowding, spectral resolution used, and importance of spectral resolution effects. The first type of measurement, which we refer to here as narrow-band equivalent width indices, are the most familiar and have been widely used in the Lick system of spectral indicators (e.g.,

Burstein et al. 1984; Worthey et al. 1994). These Lick equivalent width indices place a bandpass of typically 30−40 Å (although some of the bluer indices have narrower bandpasses) centered on a particular spectral feature, and then use bandpasses of similar width on either side of the feature to provide a pseudo-continuum reference. Due to their relatively broad width, the pseudo-continuum bandpasses often contain fairly strong absorption lines. The second system of measurements, which have been primarily developed in Rose (1984; 1994), measure the relative depth of two neighboring features without reference to the continuum. This is accomplished by measuring the residual central intensities in the two neighboring absorption lines, and forming their ratio. Alternatively, a similar type of ratio can be measured by using two neighboring pseudo-continuum peaks in the spectrum. The term "pseudo-continuum" is employed here to emphasize that for integrated spectra of galaxies, the true continuum is rarely measured; instead a local peak is measured that comes closest to the true continuum value. We refer to these measurements as line ratio indices. A third set of measurements involve isolating the pseudo-continuum peaks on either side of the absorption feature of interest, and then directly measuring a pseudo-equivalent width. These pseudo-continuum peaks, which are apparently free of absorption lines, at the spectral resolutions typical of galaxy integrated spectroscopy, are defined either by using the pixel with the highest counts as the local pseudo-continuum peak or with an extremely narrow bandpass. In this paper we make particular use of this approach to isolate the Hγ absorption feature. Variants of this approach have been defined by Rose (1994), Jones & Worthey (1995), Vazdekis & Arimoto (1999), and Vazdekis et al. (2001b). In the latter two references, great care has been taken to minimize the effect of spectral resolution on the index, which is a major problem for this kind of index (i.e., a pseudo-equivalent width is highly sensitive to slight changes in spectral resolution). In Vazdekis et al. (2001b), the metallicity sensitivity of the index is reduced as well, by partially covering the neighboring metallic line centered on λ 4352 Å. This newest refinement on measuring the strength of Hγ is referred to as the H$\gamma_{\sigma<130}$ index.

3.1.1. Errors in Spectral Indices

Errors in the observed spectral indices can arise from limitations in photon statistics, read noise, and flat field accuracy as well as from systematics of subtracting the sky background. The optimal means of assessing the random errors in spectral indices is from the scatter in values in repeat observations. For the nucleus of M32 we have eight 4-minute exposures, and thus can establish a robust determination of the standard error in the mean index from the rms scatter. Outside the nucleus, for each extraction at a different radial distance we have divided the long-slit observations into two non-overlapping regions on either side of the peak in the light profile. We have then computed the rms scatter in each spectral index from the pairs of observations on opposite sides of the nucleus of M32 at the various radial positions. Thus for each index we have an assessment of the random errors at each slit position outside the nucleus from the scatter in only two independent measurements. Hence, the error for a particular index at a particular radial position has a considerable uncertainty from the above approach. Alternatively, we have computed

the errors in spectral indices on the basis of pure photon statistics and read noise in the CCD. While this approach is far more reliable statistically, it provides a less comprehensive assessment of total uncertainties in the measurements. Fortunately, we find that on average the photon statistical errors are generally consistent with the observed scatter from the paired observations. As a result, the $\pm 1\sigma$ errors on spectral indices cited in Tables 2 and 3 are the more statistically secure errors derived from photon statistics.

We also calculated the potential effect of errors produced by uncertainties in the background subtraction. All data reduction procedures as described above were repeated with the sky exposures both enhanced and reduced by 10%. The spectral indices were recalculated with the modified sky background subtraction, and the rms scatter between the results obtained with enhanced and reduced sky values was calculated for each index. The result is that even for the largest off-nuclear radial position, the average error introduced by mis-subtraction of sky is significantly less than the errors from photon statistics. Thus, even at the furthest radial position, and with a generous evaluation of the sky background uncertainty, the errors from uncertain sky removal are considerably less than the random errors. At smaller radial distances, the sky errors will clearly be of even less significance. The one serious problem involved with background subtraction occurs if the slit for the "sky" exposure or for the M32 exposure intersects a faint HII region in the disk of M31 an/or a planetary nebula in M32 or M31. The result is contamination of the Balmer lines with emission. We have in fact mentioned such problems, both on the central Subaru slit (two PNe on the slit) and on a Tillinghast/FAST background exposure.

Data on the spectral indices and their errors for the different radial slit positions in M32 are listed in Table 2 for the Subaru/FOCAS data and in Table 3 for the Tillinghast/FAST data.

3.2. Population Synthesis Methods

A comparison of the observed index strengths to those predicted by stellar population synthesis models allow us to make a quantitative statement on the radial age/metallicity changes in M32. The most popular approach followed by these models is to predict the strengths of the strongest absorption features in galaxy spectra (Worthey 1994; Vazdekis et al. 1996). These models make use of polynomial fitting functions which relate the strengths of these features to stellar atmospheric parameters (i.e., T_{eff}, log g, and [Fe/H]) on the basis of the Lick/IDS stellar spectral library (Gorgas et al. 1993; Worthey et al. 1994). A number of shortcomings of this approach prevent us from fully exploiting the information present in the high quality spectra of M32. Among these problems is the fact that the spectral resolution of these models (FWHM>8.5 Å) is much lower than that intrinsic to M32. Moreover, the bluer the wavelength the lower the resolution (e.g., FWHM$\sim$11.5 Å for $\lambda \sim$4000 Å) (see Worthey & Ottaviani 1997). Also, the fact that the Lick/IDS stellar library was not flux-calibrated forces us to transform our data to the Lick/IDS instrumental response curve to be able to compare the model predictions with the measured line-strengths. In addition, since these models only predict a specified number of spectral indices rather than the full

spectra, we would be throwing away much of the information present in the M32 spectra, which is contained in the weaker spectral lines.

A further step in the modelling has been recently achieved by synthesizing full spectral energy distributions (SEDs) for old-age single burst stellar populations (SSPs) at a spectral resolution with FWHM=1.8Å (Vazdekis 1999; Schiavon, Barbuy, & Bruzual 2000; Schiavon 2004) and flux-calibrated response. These newly developed models are based on the JCFSL, i.e., the extensive empirical stellar spectral library of Jones (1999) that we have described above. This new approach (see also Bruzual & Charlot 2003) allows us to analyze a galaxy spectrum at a spectral resolution limited only by its dynamics (i.e., its velocity dispersion, to which the model spectra should be smoothed). Thus, all the indices described in §3.1 can be measured directly on the model SEDs. It is worth recalling that, thereafter, when we refer to the Lick indices we are not meaning those indices predicted by the previous models (with the specific instrumental response curve and resolutions of the Lick/IDS system), but we use the Lick index definitions for measuring these indices on the smoothed model SEDs (i.e., with flux-calibrated response and the resolution of M32).

In this paper we make use of two sets of models that differ in their essential ingredients. Whereas those of Vazdekis (1999) (as recently updated in Vazdekis et al. 2003) make use of the latest version of the Padua isochrones (Girardi et al. 2000), that of Schiavon (2004) uses the same isochrones and a new set of fitting functions to Lick/IDS indices. Furthermore, Vazdekis (1999) transforms the theoretical parameters of these isochrones to the observational plane following empirical stellar libraries such as those of Alonso, Arribas, & Martinez-Roger (1996,1999) whereas Schiavon (2004) adopts the same calibrations for F, G and K stars, and calibrations by Westera et al. (2002) for cooler and hotter stars. All of these models make use of scaled solar isochrones, thus do not directly model the non-solar abundance ratios found below.

4. Radial Population Trends in M32

4.1. Evidence for an Age and Metal-Abundance Gradient

The central question of this paper is whether a population gradient is present within the inner 30″ (∼100 pc of M32. We address this issue in Figs. 1 and 2, where spectral index data from the Subaru and Tillinghast/FAST observations, respectively, are plotted as a function of radial distance from the nucleus of M32. To best disentangle age from metallicity effects, we have plotted spectral indices that measure the primarily age sensitive Balmer lines versus an index that primarily responds to mean metallicity. Specifically, in Figs. 1 and 2 the right hand panel is a plot of the Lick Hβ index versus the [MgFe] index, while the left panel is a plot of the Vazdekis et al. (2001b) H$\gamma_{\sigma<130}$ index versus the same metallicity sensitive [MgFe] index. The [MgFe] index is a composite of both Fe-dominated absorption lines and the 5175 Å feature of the α-element Mg, as defined in González (1993; [MgFe] = $\sqrt{Mg\ b \times (Fe5270 + Fe5335)/2}$), thus providing an assessment of the overall heavy element abundance. In fact, Thomas, Maraston, & Bender (2003) find it to be such

a good tracer of overall metallicity that it is essentially independent of [α/Fe] (see also Bruzual & Charlot 2003; Vazdekis et al. 2001a). In both plots we have included a grid of indices based on the previously described single stellar population models of Vazdekis (1999, and updated in Vazdekis et al. 2003) that cover a range in age and [Fe/H]. The primarily horizontal lines connect models with the same age while the primarily vertical lines connect models with the same [Fe/H].

The main result of Figs. 1 and 2 is that a small age and metallicity trend does indeed exist within the central $\sim$30″ (1 R_e) of M32, in the sense that the age increases from the center outward while the metallicity slightly decreases. Specifically, from the Subaru data plotted in Fig. 1 it is evident that the light-weighted mean age increases from $\sim$3$-$4 Gyr in the nucleus to $\sim$6$-$7 Gyr at $\sim$30″ radius, while the light-weighted mean metallicity (as measured by [MgFe]) decreases from almost exactly solar in the nucleus to ~-0.3 at 30″. There is good agreement between the results obtained from the Hβ index and those from the H$\gamma_{\sigma<130}$ index. The FAST data, plotted in Fig. 2, provides similar results, particularly with regard to the Hβ versus [MgFe] plot. The trend in H$\gamma_{\sigma<130}$ versus [MgFe] is less convincing, likely due to the lower S/N ratio of the Tillinghast/FAST data.

The overall trend in mean metallicity, as defined by [MgFe], can be further refined to individual elements. In Figs. 3, 4, 5, and 6 we plot the Hβ and H$\gamma_{\sigma<130}$ indices versus the Lick Fe3 (where Fe3 = (Fe4383+Fe5270+Fe5335)/3) , Mg b, CN2, and G4300 indices, respectively, for the Subaru data. Overall, the basic trend of decreasing metal abundance with increasing radius is apparent. However, as has been discussed in Schiavon et al. (2004) and Worthey (2004), there are zero point differences from one metal indicator to another with respect to the models that indicate slight departures from a solar abundance ratio pattern in M32. Specifically, the central values in M32 indicate that [Fe/H]$\sim=+0.1$ (as seen in the Fe3 index in Fig. 3), while [Mg/H]$\sim=-0.1$ (Fig. 4), and the data for the CN2 index (Fig. 5) indicates that [C+N/H]$\sim+0.1$. In Fig. 6 the central value of the G-band, as characterized by the G4300 index, implies that [C/H]~-0.2. In addition, the size of the radial gradient is different in some features, indicating that there is a radial trend in abundance patterns as well. We illustrate this fact in the case of [Mg/Fe] by plotting the Mg b index versus Fe3 in Fig. 7. The M32 nucleus is clearly shifted from the grid of solar abundance ratio models in the plot, in the sense that Mg b is too weak for the given Fe line strength. However, at larger radial distances there is a systematic shift of the M32 data towards the model grid, indicating that [Mg/Fe] outside the nucleus shifts closer to the solar abundance ratio. We quantify the shift in [Mg/Fe] using the following procedure. Since the Mg b index is dominated by Mg and the Fe3 index by Fe (Tripicco & Bell 1995), we can extract approximate abundances for [Mg/H] and [Fe/H] from the respective indices. Specifically, plots of Mg b versus both Hβ and H$\gamma_{\sigma<130}$ provide nearly orthogonal age versus metallicity model grids, allowing for a convenient approximation of [Mg/H] (cf., Fig. 4). Similarly, plots of Fe3 versus both Hβ and H$\gamma_{\sigma<130}$ provide an approximation of [Fe/H] (cf., Fig. 3). From the two individual abundances we then infer [Mg/Fe]. Taken at face value, we find an increase in [Mg/Fe] from -0.25 in the center of M32 to -0.08 at 30″ radius. Note that an alternative approach for obtaining the [Mg/Fe] ratios can be followed using models specifically

computed for different α-enhancements (e.g. Trager et al. 2000; Thomas et al. 2003), on the basis of the sensitivities of these lines to the abundance changes of the different species as tabulated in Tripicco & Bell (1995).

The lower S/N ratio FAST data, not plotted, shows essentially the same abundance patterns and trends as for the Subaru data. The slight enhancement of Fe above solar, along with the underabundance of Mg and overabundance of CN with respect to solar, have also been reported in Schiavon et al. (2004), based upon the same FAST data as used here, but incorporating Schiavon's (2004) population synthesis models.

To further illustrate the changing absorption line strengths with radius, in Fig. 8 we have plotted the ratio between the spectrum at $\sim$30″ and that in the nucleus. As can be seen in the ratio spectrum, all major spectral features, including Ca II H and K and the Balmer lines Hδ, Hγ, and Hβ, appear in emission, indicating that these features are deeper in the nuclear spectrum, as is expected if the central population of M32 is both older and more metal-rich than at 30″. That is, the smaller (in equivalent width) Balmer lines at larger radial distance reflect an older age.

4.2. Effect of Scattered Light on Observed Line Strength Gradients

While the Subaru and Tillinghast/FAST data indicate only a very modest trend in age and metal-abundance in the central 30″ of M32, the KPNO 4-m data present a very different story. In Fig. 9 the KPNO data are plotted for a variety of spectral indicators versus the H$\gamma_{\sigma<130}$ age indicator. The Vazdekis model grids are again plotted, as in the previous Figs. Also plotted, as a representative population with age $\sim$12 Gyr and [Fe/H]~-0.7, is the integrated spectrum of the Galactic globular cluster 47 Tucanae. The KPNO data indicate a strong radial age and metallicity gradient in M32, with the central age and metallicity in agreement with that found in the Subaru and FAST data, but with the data at 30″ radius apparently having about the same age and metallicity as 47 Tuc. Thus the KPNO 4-m results are in striking disagreement with those found from the Subaru and Tillinghast/FAST data, in that the gradient seen in the KPNO data is much more pronounced than that found in the Subaru and FAST data.

A clue to understanding the large apparent line strength gradients in the KPNO data is present in the behavior of the deepest lines in the spectrum, i.e., the Ca II H and K lines. Since the integrated spectrum of M32 is overwhelmingly dominated by cool stars, as is demonstrated below in §4.4, the depths of the Ca II H and K lines should not vary appreciably with distance from the nucleus. Instead, these lines have substantially lower depths in the nucleus as opposed to in the outer regions, as is illustrated in Fig. 10, where the spectrum at 30″ outside the nucleus is normalized to and overplotted on the nuclear spectrum. We quantify the difference in Ca II H and K line depths seen in Fig. 10 by using the pseudocontinuum peaks just shortward of Ca II K and longward of Ca II H as references. Specifically, the mean ratio between the line depth and neighboring pseudocontinuum peak is 67% smaller in the nucleus of M32 than it is at 30″ outside

the nucleus.

The elevated appearence of the Ca II line bottoms in the outer region spectrum indciates that the Ca II lines (as well as all other spectral features) are diluted by scattered light in the spectrograph. Specifically, we speculate that scattered light from the semi-stellar nucelus of M32, which reaches a peak flux ∼100 times higher than at 30″ radius, contaminates the spectrum at larger radii. To further assess this conjecture we have generated a featureless continuum with the same spectral response as for the raw observed spectrum of the M32 nucleus. We chose the scattered light component in this manner because analysis of the scattered light spectrum of a star, HD187691, taken on the same night as the M32 data shows the spectrum of the scattered light ot be a highly diluted version of the star's spectrum, with a raw flux distribution roughly similar to that of the star. We added the above featureless continuum in varying amounts to the M32 nuclear spectrum, up to a level that reproduces the line depths in Ca II H and K at 30″ radius. We have measured spectral indices in these artificially diluted spectra of M32, and find that the entire radial population gradient in the KPNO 4-m data can be accounted for by scattered light contamination. The results of the scattered light simulation are plotted in Fig. 11, where the actual observed and simulated data are seen to overlap fully. Basically, dilution by scattered light weakens all spectral features, including both Balmer lines and metal lines. Hence, one would expect scattered light to produce an artificially older and more metal-poor spectrum, as is measured in the KPNO 4-m data.

Given the evident problem of scattered light in the KPNO 4-m data, can we be sure that the more modest detected trend towards older and more metal-poor mean population in M32 with increasing radius in the Tillinghast/FAST and Subaru data is not also a spurious result? We argue that the FAST and Subaru data are free from scattered light problems becasue we have offset the slit from the nucleus in the long exposure spectra which are used to extract information at larger radii. This is especially true for the FAST data, where we have obtained spectra with the slit offset by 5″, 15″, and 30″ from the nucleus, so that our results always refer to spectra that are extracted from regions where the flux is at the highest levels. Clearly, the greatest scattered light problem arises when the nucleus, which is 100 times brighter than at 30″ radius, is positioned on the slit. Given the excellent agreement between the Subaru and FAST data, we expect that by removing the nucleus from the slit in both datasets, we have basically alleviated the scattered light problem entirely.

To summarize, we have found a modest, but significant, radial population trend in the central region of M32, such that the light-weighted mean age and metallicity of M32 goes from ∼3−4 Gyr and [MgFe]=0.0 in the nucleus to ∼6−7 Gyr and [MgFe]=−0.3 at 30″ radius. A much stronger radial population trend seen in the 4-m data is found to be an artifact of scattered light in the spectra, produced by the location of the bright semi-stellar nucleus of M32 on the spectrograph slit.

4.3. Comparison with the Results of Worthey (2004)

In a recent preprint, Worthey (2004) also has obtained long-slit spectra for M32, out to ∼45″ radius. He finds the mean age and metallicity for the nucleus of M32 to be 4 Gyr and +0.05, which is consistent with our nuclear results. He also finds that the mean age increases by a factor of 2.5 from the nucleus to 1 R_e, while the abundance drops by 0.3 dex. Again, our results are in good agreement with Worthey's, since we find the age to increase by a factor 2, and abundance to decrease by 0.25 dex. In addition, Worthey (2004) finds that [Mg/Fe] is underabundant by ∼−0.1, which is very close to our mean value of ∼−0.15. However, he does not report a radial gradient in [Mg/Fe] (we find that [Mg/Fe] inceases from −0.25 at the nucleus to −0.08 at 1 R_e). Finally, Worthey (2004) reports that CN indices actually increase from the nucleus out to a maximum at 4″ radius before dropping at larger radii. We instead see a monotonic decrease in CN from the nucleus outward. On the whole, the two studies are in excellent accord.

4.4. Limits on the Role of Hot Stars

The above results, taken at face value, indicate a ∼3 Gyr age gradient within the central 30″ of M32. However, it has been pointed out previously (e.g., Maraston & Thomas 2000; de Propris 2000; Brown et al. 2000) that a relatively small population of hot stars (i.e., from a young hot star population, a metal-poor population, or a blue straggler population), if present in early-type galaxies, could "contaminate" the integrated spectrum, thereby producing articially young light-weighted mean ages from models which lack that component. Thus we now consider whether the apparent age gradient in M32, from ∼4 Gyr in the center to ∼7 Gyr at 30″ radius, could instead result from the changing influence of a relatively small hot population. To explain our case, there must exist a hot component in the center of M32 that is less prevalent as one goes radially outward from the nucleus.

The hot star hypothesis can be tested by examining the behavior of the Ca II index that was originally utilized by Rose (1985; 1994) and more extensively modelled in Caldwell, Rose, & Concannon (2003) and Leonardi & Rose (2003). The Ca II index, which is basically constant in cool stars, declines very steeply towards early F and A stars as Ca II H and K disappear and Hϵ (which is coincident in wavelength with Ca II H) increases in strength towards the higher temperature stars. Specifically, the decline in the Ca II index sets in at T_{eff} above ∼8000 K for solar abundance stars. As is summarized in Rose (1985; 1994) and Caldwell, Rose, & Concannon (2003), a small deficit in the Ca II index, compared with the "expected" value of 1.20 for a strictly old population, is observed in the nucleus of M32. The deficit of ∼0.05 from the "expected" value indicates that ∼3% of the light at 4000 Å in M32 is provided by hot (i.e., A-type) stars. This population fails by a factor of 5 to account for the overall strong Balmer lines observed in M32, i.e., an intermediate-age (∼4 Gyr old) population is required to explain the integrated spectrum of M32. Here we consider whether a gradient in the hot population might provide an explanation for the ∼3 Gyr age gradient

observed in the central 30″ of M32.

Unfortunately, the Subaru spectra do not extend blueward enough to provide coverage of Ca II K, and the KPNO 4-m spectra are compromised by scattered light, hence we rely exclusively on the FAST data. The Ca II index at various radii in M32 is plotted in Fig 12. Within the observational errors the Ca II index is seen to be roughly constant, indicating that the ∼0.05 deficit in the index due to a hot star population is present in essentially constant proportion from the nucleus through a radius of 30″. To realize the implication of the small, constant Ca II deficit in M32, we have done the following exercise. We have both added and subtracted in varying amounts the spectrum of the A4V star HD136729 to the central Tillinghast/FAST spectrum of M32. Here we have used the spectrum of HD136729 available in the IUCFSL, and have rebinned it and smoothed it to match that of the M32 data. We have also normalized the HD136729 to that of M32 at 4000 Å. Specifically, we added and subtracted the spectrum of HD136729 at 5%, 10%, and 20% of the level of M32 (at 4000 Å). The effect on the Ca II index of M32 can be seen in Fig 12. Subtracting or adding only a 5% contribution from HD136729 at 4000 Å changes the Ca II index of M32 by ±0.09, which is substantially higher than the observed deficit of ∼0.05 of M32 from the "standard" value of 1.2 for an entirely cool star population. Thus only ∼3% of the light at 4000 Å in M32 comes from hot stars. Furthermore, this contribution is constant to within ∼±0.02 in the Ca II index over the central 30″ of M32. If we now consider the impact of a 3% contribution of A4V light at 4000 Å on the Hβ index, we find that the Hβ index changes by only ±0.09 as the 3% A4 star contribution is added and subtracted. As can be seen in Fig. 1, a change in Hβ of 0.09 produces only a tiny effect on the derived age. Given that we find the Ca II index to vary radially by less then 0.02, we thus infer that a gradient in Hβ due to a gradient in hot star contribution can be present at no more than the 0.04 level in that index, which is far below the observed Hβ radial gradient of ∼0.4.

Finally, we have repeated the above analysis using the solar abundance 0.32 Gyr model population from Vazdekis (1999), and obtain very similar results as were obtained with the A4V star, since the 0.32 Gyr model spectrum is similar to that of the A4V star HD136729 in the blue. Thus we also conclude that at most only ∼3% of the light at 4000 Å in M32 comes from a ∼0.3 Gyr population.

4.5. Limits on Contamination from Emission Lines

Another important issue to consider is the possibility that contamination from emission lines could be systematically affecting the results derived from the absorption line indices. The most obvious concern is emission fill-in for the Balmer lines. Here we are primarily interested in the potential effect of a radial *gradient* in emission producing spurious population effects. Since the data indicate that age systematically increases with increasing radial distance from the center of M32, we must assume then that emission contamination also increases with radial distance, if it is producing a spurious age increase due to emission fill-in of the Balmer lines. Such a scenario is perhaps somewhat contrived, in that one might expect such emission to be centrally concentrated,

but we will consider that possibility nonetheless.

There are three potential sources of emission contamination. The first occurs if the spectrograph slit intersects a planetary nebula either, in M32 or M31, and can contaminate either the slit position through M32 or the offset "sky" slit position. The second possibility is that the slit can be positioned on an HII region in M31. Again, this could be either the slit positioned on M32 or at the offset sky position. Finally, there can in principle be a weak AGN emission spectrum in the nucleus of M32.

All three sources of emission are plausible problems. Ciardullo et al. (1989) report positions for seven planetary nebulae (PNe) within the central 30″ of M32. As mentioned earlier, the Subaru spectrum through the nucleus of M32, at a PA of 80°E of N in fact intersect two of these PNe's, #24 and 25 in the Ciardullo et al. (1989) Table 6. Inclusion of these two PNe lead to a very significant fill-in of the Balmer lines at 10″ radius. We have also found that a sky position for spectra taken of M32 with the FLWO 1.5-m and the FAST spectrograph that are not used in this paper is contaminated with a faint HII region from the M31 disk on part of the slit. In that case we observed an unexpected enhancement in the Hβ absoprtion strength in M32, since Hβ absorption in our sky position was artificially lowered due to fill-in from the HII region emission. Finally, M32 is known to harbor a central mass concentration (Tonry 1984; Dressler & Richstone 1988; van der Marel et al. 1994, 1998; Verolme et al. 2002). Thus an AGN spectrum is not unexpected.

The possibility that emission fill-in is an important effect in the nucleus of M32 (and for other low-luminosity early-type galaxies) has been discussed in Jones (1999). Here we briefly summarize the conclusions. González (1993) detected a slight amount (0.11 Å in equivalent width) of [OIII]λ5007 emission in the nuclear spectrum of M32. Jones's (1999) spectra do not cover [OIII]λ5007, but provide tight upper limits on [OII]λ3727, from which strong constraints can be set on the type of emission spectrum that is contributing to M32. In particular, a LINER spectrum is decisively ruled out, since, based on the observed [OIII]λ5007 emission of 0.11 Å in equivalent width found by González (1993), one predicts an equivalent width of [OII]λ3727 in excess of the observed upper limit. Instead, the two possibilities that remain are either planetary nebula emission or emission from an HII region. In both cases, the amount of emission predicted at Hγ from the small [OIII]λ5007 detection by González (1993), is only 0.008 Å in the planetary nebula case and 0.005 Å in the HII region case, which leads to an age adjustment of $<$1 Gyr. Note that the adjustment is such that emission tends to make the galaxy look *older* than it actually is.

We have reinvestigated the nuclear spectrum of M32 using the eight 4-minute exposures acquired with the FAST spectrograph. These spectra cover both [OIII]λ5007 and [OII]λ3727. A key issue in emission line detection is to find an appropriate template spectrum, which matches the absorption features of M32 but is certified to be without emission contamination itself. For a template we have used the synthesized integrated spectrum of the Galactic cluster M67 from Schiavon et al. (2004). In the Schiavon et al. (2004) paper M67 was found to have a very similar age and chemical composition to the luminosity-weighted mean age and metallicity of M32. Since the M67

integrated spectrum is built up from coadding spectra of individual stars in M67, the resultant integrated spectrum is certainly free from emission. In addition, the M67 spectra were acquired with the same FAST spectrograph and grating combination as for M32. We have registered the M67 spectrum to that of M32 and formed the ratio spectrum between the two. The ratio spectrum is plotted in the region of [OII]λ5007 and [OIII]λ3727 in Figs. 13 and 14 respectively. We do not see any conclusive signs of either [OIII]λ5007 or [OII]λ3727. Rather, we establish an upper limit to the equivalent width of [OIII]λ5007 of 0.05 Å, and a limit to [OII]λ3727 of 0.15 Å. The fact that our upper limit on [OIII]λ5007 conflicts with the detection by González (1993) can be due to the different apertures used for the "nucleus" of M32. In any case, emission contamination of the Balmer lines in the center of M32 is small.

Given that we have established the nuclear spectrum of M32 to contain little or no emission contamination, we now use the nuclear spectrum of M32 as a template and divide it into the other spectra extracted at different radii. We then look for [OII]λ3727 and [OIII]λ5007 emission in these template-normalized spectra. Due to the radial gradient in the absorption spectrum of M32, using the nuclear spectrum of M32 as a template is not completely successful at cleanly removing the underlying absorption spectrum in the neighborhood of [OII]λ3727 and [OIII]λ5007 at extra-nuclear positions in M32. This problem is particularly apparent at the blue end of the spectrum, where all of the key spectral features (such as Ca II H and K) appear in emission, since they are deeper in the M32 nucleus, as well as in the Balmer lines. However, applying a conservative upper limit defined from the spurious peaks in the neighborhood of [OII]λ3727 we conclude that the equivalent width of [OII]λ3727 emission is below 0.2 Å FWHM at all locations along the slit out to $\sim$30″, and the limit on [OIII]λ5007 is $\sim$0.05 Å. For high-excitation emission spectra, such as from PNe and metal-poor HII regions, the limit on [OIII]λ5007 emission produces a stringent limit on Hβ emission. On the other hand, for low-excitation HII regions, the [OII]λ3727 emission exceeds Hβ emission, thus the limit on [OII]λ3727 emission produces a strict limit on Hβ emission. In short, we find that emission line fill-in in the outer region of M32 cannot account for the observed age and metallicity trend with radius. As well, if the gradient were due to discrete PNe and/or HII regions on the slit, we would readily detect them on the original two-dimensional spectra, as we have done in a couple of cases.

5. Discussion

The results from the previous section suggest that there is a radial gradient in the mean age and metallicity in the central regions of M32, such that the mean age rises from $\sim$3$-$4 Gyr in the nucleus to $\sim$6$-$7 Gyr at 30″ radius, while the metallicity drops from [Fe/H]$\sim$0.0 to $\sim-$0.3. In addition, we infer a slight gradient in [Mg/Fe] such that [Mg/Fe] increases from $-$0.25 in the nucleus to $-$0.08 at 30″ radius. These age and chemical enrichment trends all point towards a more extended history of star formation and chemical enrichment in the nucleus of M32 than at 1 R_e. Of particular note is that the higher mean overall metallicity in the center of M32, coupled with

the lower ratio of the α-element Mg relative to Fe, imply both a greater chemical enrichment in the nucleus as well as a longer time period for that enrichment, since [α/Fe] may be a reflection of relative timescales of Type II versus Type Ia supernovae. In short, a consistent picture of the radial line strength trends in M32 emerges from this study.

As was mentioned in the Introduction, no gradient in broad passband colors has been found for the central regions of M32 in either the optical or IR (Peletier 1993), which appears to contradict the distinct age/metallicity gradient found in our spectra. However, the trend is towards older age and lower metal-abundance as one proceeds radially outward. An increase in age produces a reddening of colors while the decrease in metallicity has the opposite effect. Thus we have the interesting situation in which the competing effects of age and metallicity lead to no variation in optical/IR colors. To investigate the plausibility of this assertion, we have assessed the B−V and U−B colors predicted from our stellar population models. The model B−V color for a 4 Gyr solar abundance population is 0.89, as opposed to 0.86 for a 7 Gyr, [Fe/H]=−0.3 population. Thus the radial change in color is very small and difficult to detect. For U−B the model color shifts from 0.44 to 0.37 from the younger to the older population, which is again a small shift, but perhaps should be detectable. We note, however, that our models are based on the clear oversimplification of a single population at each radius that is entirely at the luminosity-weighted mean value, while in reality there must be a spread in both age and metallicity. In addition, our models are basically limited to solar abundance ratios, while our data for M32 indicates departures from that pattern. In fact, while the model B−V color for the center of M32 is consistent with the observed color, to within the uncertainties of Galactic reddening in that direction, the model U−B colors are systematically bluer than the observed colors reported in Peletier (1993) by ∼0.1−0.15. We also note that some spectral features, e.g., Mg b, also show no significant line strength gradient, again because an older population tends to have stronger Mg b, while a more metal-poor population tends to have weaker Mg b, as can be seen in Fig. 4. Hence the most striking line strength gradients that we observe are in the Balmer lines.

It is important to bear in mind that the above inferences about radial population trends are for the light-weighted mean population. An alternative scenario to the possibility of an overall shift of the bulk of the population to a younger age, as one proceeds to smaller radii, is to invoke a shifting balance between two populations. Specifically, one can speculate that there was an initial star formation episode ∼11 Gyr ago, as suggested by the presence of blue horizontal branch stars in color-magnitude diagrams derived from HST images (Ikuta 2001; Alonso-Garcia et al. 2003), as well as a more recent, higher metallicity, star formation episode perhaps 2−3 Gyr ago. The observed population trend can then be seen as a higher concentration of the younger population in the center of M32. Such a population structure would in fact be a natural result of the scenario proposed by Bekki et al. (2001), in which centralized star formation in M32 is triggered by the tidal field of M31. To discriminate between a mean trend and a changing balance between two populations is beyond the scope of this paper. It should be kept in mind that the more complex modelling involved with a two-population scenario could as well impact the details of conclusions

about the small gradient in non-solar abundance ratios (viz., in [Mg/Fe]) found earlier. Note that in any case the younger population cannot be any younger than ∼2 Gyr, or it would produce a strong signature in the Ca II index discussed in §4.4.

Finally, we return to the issue of scattered light in M32. In the Introduction we mentioned the conflicting results of several previous long-slit spectroscopic studies of M32. Most, if not all, of these studies involve spectra taken with the slit passing through the nucleus of M32, hence they are particularly vulnerable to effects of scattered light. Perhaps the major discrepancies between studies are due to varying degrees of scattered light. In addition, while M32 represents an especially pathological case of a bright nucleus as a source of scattered light, it is not inconceivable that studies of radial population gradients in other early-type galaxies can have been compromised by scattered light as well.

We wish to thank S. M. Faber for the crucial suggestion of scattered light as a source of spurious age/metallicity gradients in M32. Thanks are also due to Dr. R. Peletier and Drs. C. Ikuta for their efforts in securing the Subaru/FOCAS observations. This research has been partially supported by NSF grant AST-9900720 to the University of North Carolina. It has also been supported in part by a Grant-in-Aid for Scientific Research by the Japanese Ministry of Education, Culture, Sports, Science and Technology (No. 13640230).

REFERENCES

Abadi, M. G., Moore, B., & Bower, R. G. 1999, MNRAS, 308, 947

Alonso, A., Arribas, S., Martinez-Roger, C, 1996, A&A, 313, 873

Alonso, A., Arribas, S., Martinez-Roger, C, 1999, A&A, 140, 261

Alonso-Garcia, J., Mateo, M., & Worthey, G. 2003, AJ, 127, 868

Balcells, M., & Peletier, R. F. 1994, AJ, 107, 135

Bekki, K., Couch, W. J., Drinkwater, M. J., & Gregg, M. D. 2001, ApJ, 557, L39

Bertelli, G., Bressan, A., Chiosi, C., Fagotto, F., & Nasi, E. 1994, A&AS, 106, 275

Brown, T. M., Ferguson, H. C., Stanford, S. A., & Deharveng, J.-M. 1998, ApJ, 504, 113

Brown, T. M., Bowers, C. W., Kimble, R. A., & Sweigart, A. V. 2000, ApJ, 532, 308

Bruzual, G., & Charlot, S. 2003, MNRAS, 344, 1000

Burstein, D. 1985, PASP, 97, 89

Burstein, D., Faber, S. M., Gaskell, C. M., & Krumm, N. 1984, ApJ, 287, 586

Caldwell, N., Rose, J. A., & Concannon, K. D. 2003, AJ, 125, 2891

Cardiel, N., Gorgas, J., Cenarro, J., & González, J. J. 1998, A&AS, 127, 597

Ciardullo, R., Jacoby, G. H., Ford, H. C., & Neill, J. D. 1989, ApJ, 339, 53

Choi, P. I., Guhathakurta, P., Johnston, K. V. 2002, AJ, 124, 310

Cohen, J. 1979, ApJ, 228, 405

Davidge, T. J. 1991, AJ, 101, 884

Davidge, T. J. 2000, PASP, 112, 1177

Davidge, T. J., Rigaut, F., Chun, M., Brandner, W., Potter, D., Northcutt, M., & Graves, J. E. 2000, ApJ, 545, L89

Davidge, T. J., de Robertis, M. M., & Yee, H. K. C. 1990, AJ, 100, 1143

Davidge, T. J., & Jones, J. H. 1992, AJ, 104, 1365

Davidge, T. J., & Nieto, J.-L. 1992, ApJ, 391, L13

del Burgo, C., Peletier, R. F., Vazdekis, A., Arribas, S., & Mediavilla, E. 2001, MNRAS, 321, 227

de Propris, R. 2000, MNRAS, 316, L9

de Vaucouleurs, G. 1948, Ann. d'Ap., 11, 247

Dressler, A., & Richstone, D. O. 1988, ApJ, 324, 701

Elston, R., & Silva, D. R. 1992, AJ, 104, 1360

Fabricant, D., Cheimets, P., Caldwell, N., & Geary, J. 1998, PASP, 110, 79

Fisher, D., Franx, M., & Illingworth, G. 1995, ApJ, 447, L139

Freedman, W. L. 1989, AJ, 98, 1285

Freedman, W. L. 1992, AJ, 104, 1349

Gil de Paz, A., Madore, B. F., Rich. M., Seibert, M., & GALEX Science Team 2003, BAAS, 203, 9606

Girardi, L., Bressan, A., Bertelli, G., & Chiosi, C. 2000, A&AS, 141, 371

González, J. J. PhD Thesis, University of California, Santa Cruz

Gorgas, J., Faber, S. M., Burstein, D., González, J. J., Courteau, S., & Prosser, C. 1993, ApJS, 86, 153

Gregg, M. D., Ferguson, H. C., Minniti, D., Tanvir, N., & Catchpole, R. 2004, AJ, 127, 1441

Grillmair, C. J., Lauer, T. R., Worthey, G., Faber, S. M., Freedman, W. L., Madore, B. F., Ajhar, E. A., Baum, W. A., Holtzman, J. A., Lynds, C. R., O'Neil, E. J., Jr., & Stetson, P. B. 1996, AJ, 112, 1975

Hardy, E., Couture, J., Couture, C., Joncas, G. 1994, AJ, 107, 195

Jones, L. A. 1999, PhD Thesis, University of North Carolina

Jones, L. A., & Worthey, G. 1995, ApJ, 446, L31

Kashikawa, N. et al. 2000, SPIE, 4008, 104

Kent, S. M. 1987, AJ, 94, 306

Kobayashi, C., & Arimoto, N. 1999, ApJ, 527, 573

Lauer, T. R., Faber, S. M., Ajhar, E. A., Grillmair, C. J., & Scowen, P. A. 1998, AJ, 116, 2263

Leonardi, A. J., & Rose. J. A. 2003, AJ, 126, 1811

Maraston, C., & Thomas, D. 2000, ApJ, 541, 126

Ohl, R. G., O'Connell, R. W., Bohlin, R. C., Collins, N. R., Dorman, B., Fanelli, M. N., Neff, S. G., Roberts, M. S., Smith, A. M., & Stecher, T. P. 1998, ApJ, 505, L11

Peletier, R. F. 1993, A&A, 271, 51

Rose, J. A. 1984, AJ, 89, 1238

Rose, J. A. 1985, AJ, 90, 1927

Rose, J. A. 1994, AJ, 107, 206

Rose, J. A., & Deng, S. 1999, AJ, 117, 2213

Schiavon, R. P. 2004, in preparation

Schiavon, R. P., Barbuy, B., & Bruzual, A. G. 2000, ApJ, 532, 453

Schiavon, R. P., Caldwell, N., & Rose, J. A. 2004, AJ, 127, 1513

Searle, L., & Sargent, W. L. W. 1972, ApJ, 173, 611

Thomas, D., Maraston, C., & Bender, R. 2003, MNRAS, 339, 897

Tonry, J. L. 1984, ApJ, 283, L27

Trager, S. C., Faber, S. M., Worthey, G., & González, J. J. 2000, 120, 165

Tripicco, M. J., & Bell, R. A. 1995, AJ, 110, 3035

Valdes, F., Gupta, R., Rose, J. A., Singh, H. P., & Bell, D. J. 2004, ApJS, 152, 251

van der Marel, R. P., Evans, N. W., Rix, H.-W., White, S. D. M., & de Zeeuw, T. 1994, MNRAS, 271, 99

van der Marel, R. P., Cretton, N., de Zeeuw, P. T., & Rix, H.-W. 1998, ApJ, 493, 613

Vazdekis. A., Casuso, E., Peletier, R. F., & Beckman, J. E. 1996, ApJ, 458, 533

Vazdekis, A. 1999, ApJ, 513, 224

Vazdekis, A., & Arimoto, N. 1999, ApJ, 525, 144

Vazdekis, A., Kuntschner, H., Davies, R. L., Arimoto, N., Nakamura, O., & Peletier, R. 2001a, ApJ, 551, L127

Vazdekis, A., Salaris, M., Arimoto, N., & Rose, J. A. 2001b, ApJ, 549, 274

Vazdekis, A., Cenarro, A. J., Gorgas, J., Cardiel, N., Peletier, R. F. 2003, MNRAS, 340, 1317

Verolme, E. K., Cappellari, M., Copin, Y., van der Marel, R. P., Bacon, R., Bureau, M., Davies, R. L., Miller, B. M., de Zeeuw, P. T. 2002, MNRAS, 335, 517

Westera, P., Lejeune, T., Buser, R., Cuisinier, F., & Bruzual, G. 2002, A&A, 381, 524

Worthey, G. 1994, ApJS, 95, 107

Worthey, G. 2004, AJ, (submitted)

Worthey, G., Faber, S. M., González, J. J., & Burstein, D. 1994, ApJS, 94, 687

Worthey, G., & Ottaviani, D. L. 1997, ApJS, 111, 377 White, S. D. M., & de Zeeuw, T., 1994, MNRAS, 268, 521

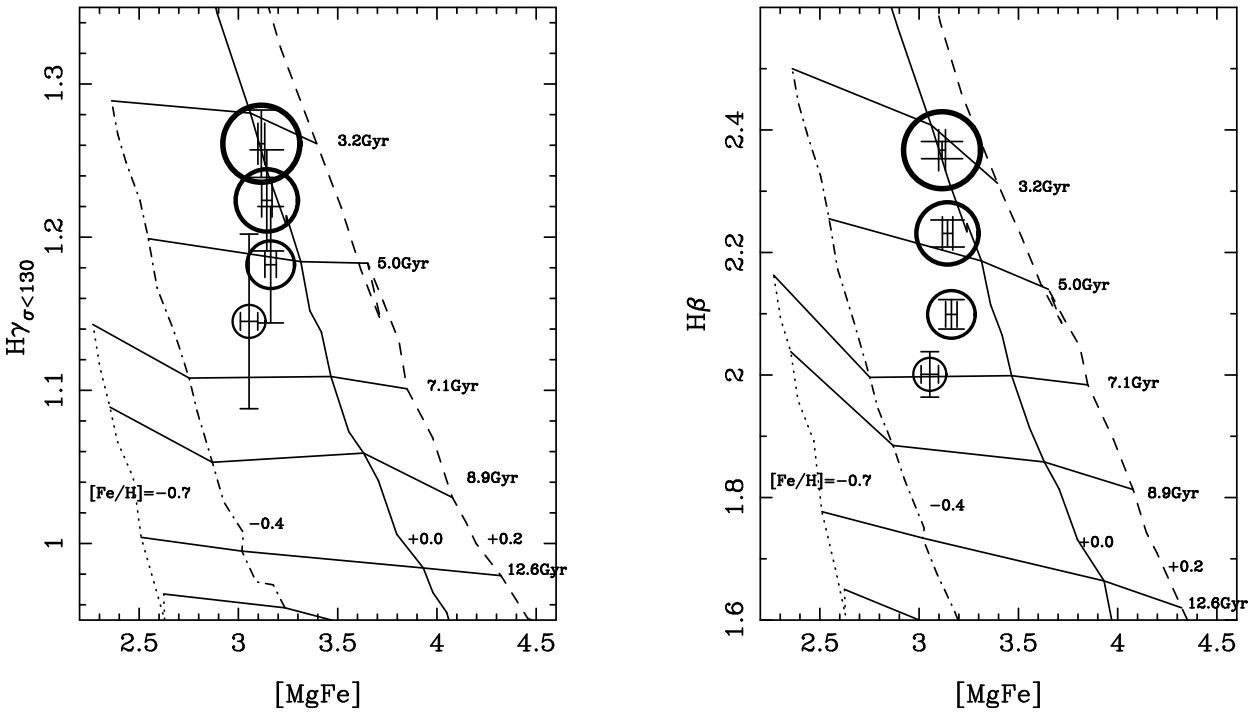

Fig. 1.— The M32 Hβ (right panel) and H$\gamma_{\sigma<130}$ (left panel) indices are plotted versus the composite [MgFe] index for the Subaru data. Overplotted on the data points are the model grid lines of constant age and [Fe/H], with constant age lines being nearly horizontal and constant [Fe/H] beng nearly vertical. The specific metallicities are, from left to right, [Fe/H]=-0.7, -0.4, 0.0, and +0.2. The ages are, bottom to top, 17.8, 12.6, 8.9, 7.1, 5.0, and 3.6 Gyr. The data points, plotted as open circles with error bars are, from largest to smallest, for the nucleus, 10″, 20″, and 30″ radial distance.

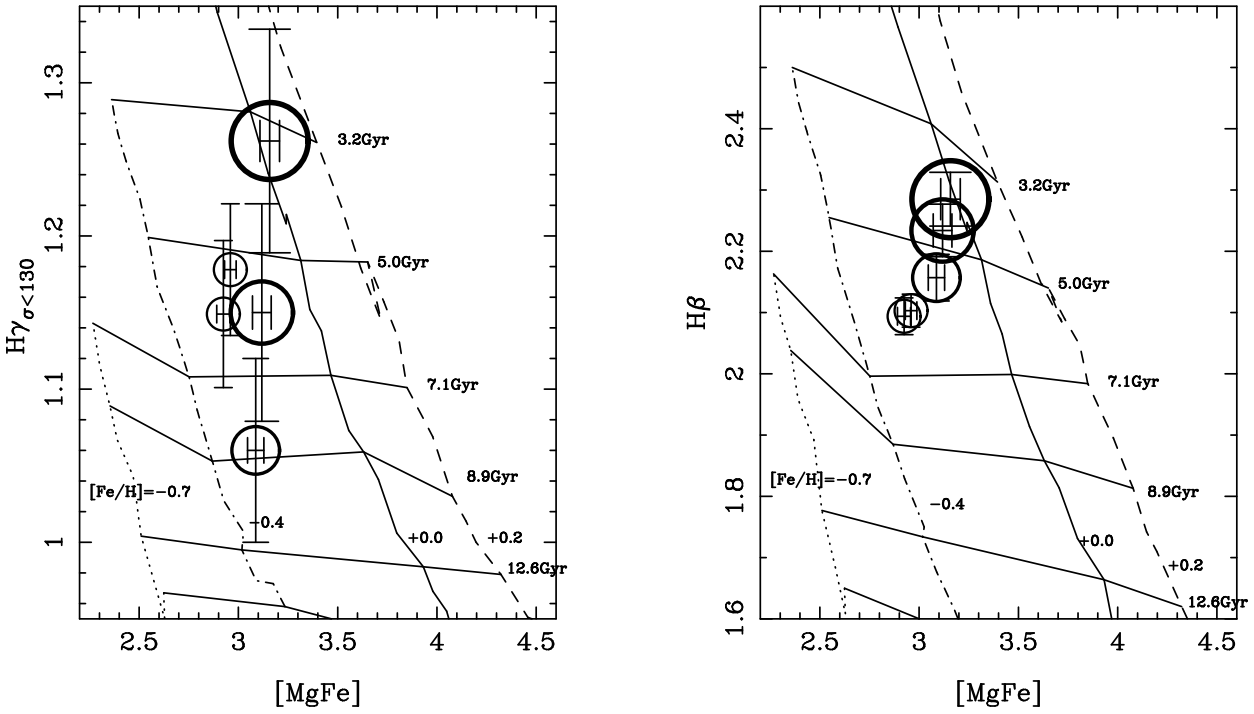

Fig. 2.— The M32 Hβ (right panel) and H$\gamma_{\sigma<130}$ (left panel) indices are plotted versus [MgFe] for the FAST data. Model grid lines are the same as for Fig. 1. The data points, again having decreasing size with larger radial distance, are at the nucleus, 7″, 19″, 35″, and 38″.

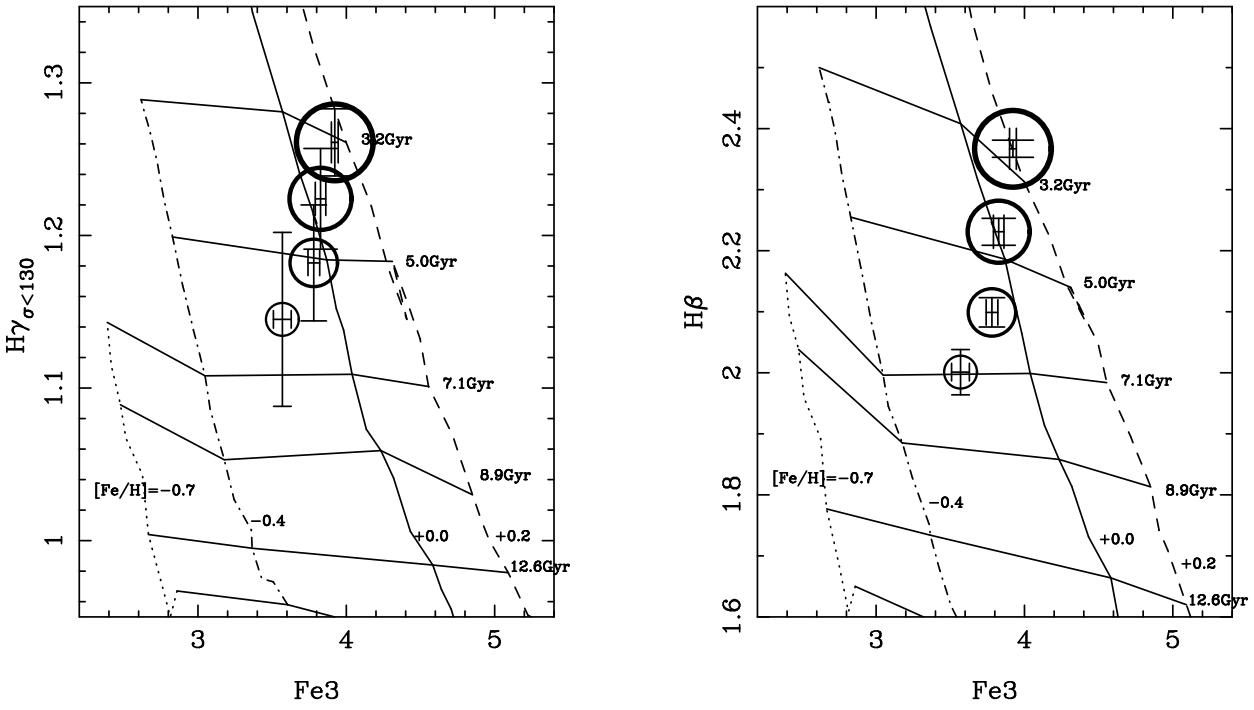

Fig. 3.— The M32 Hβ (right panel) and H$\gamma_{\sigma<130}$ (left panel) indices are plotted versus the Fe3 composite index for the Subaru data. Same symbols and models grid lines as for Fig. 1.

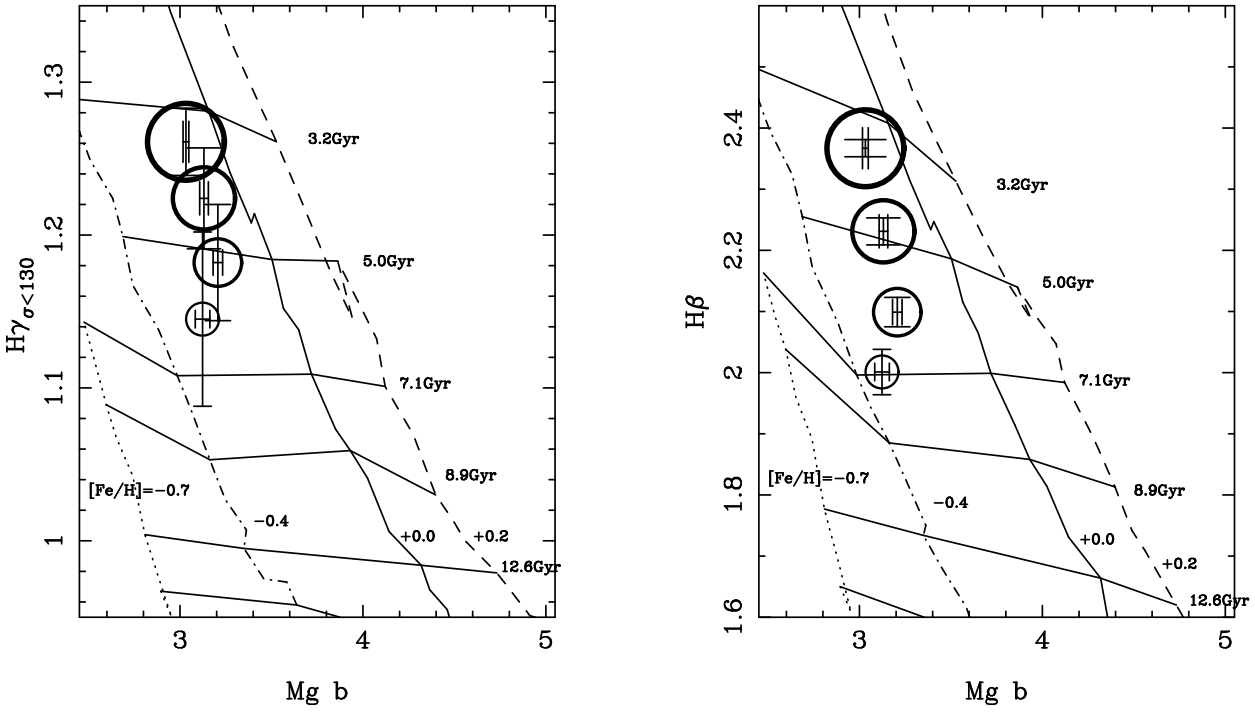

Fig. 4.— The M32 Hβ (right panel) and H$\gamma_{\sigma<130}$ (left panel) indices are plotted versus the Mg b index for the Subaru data. Same symbols and models grid lines as for Fig. 1.

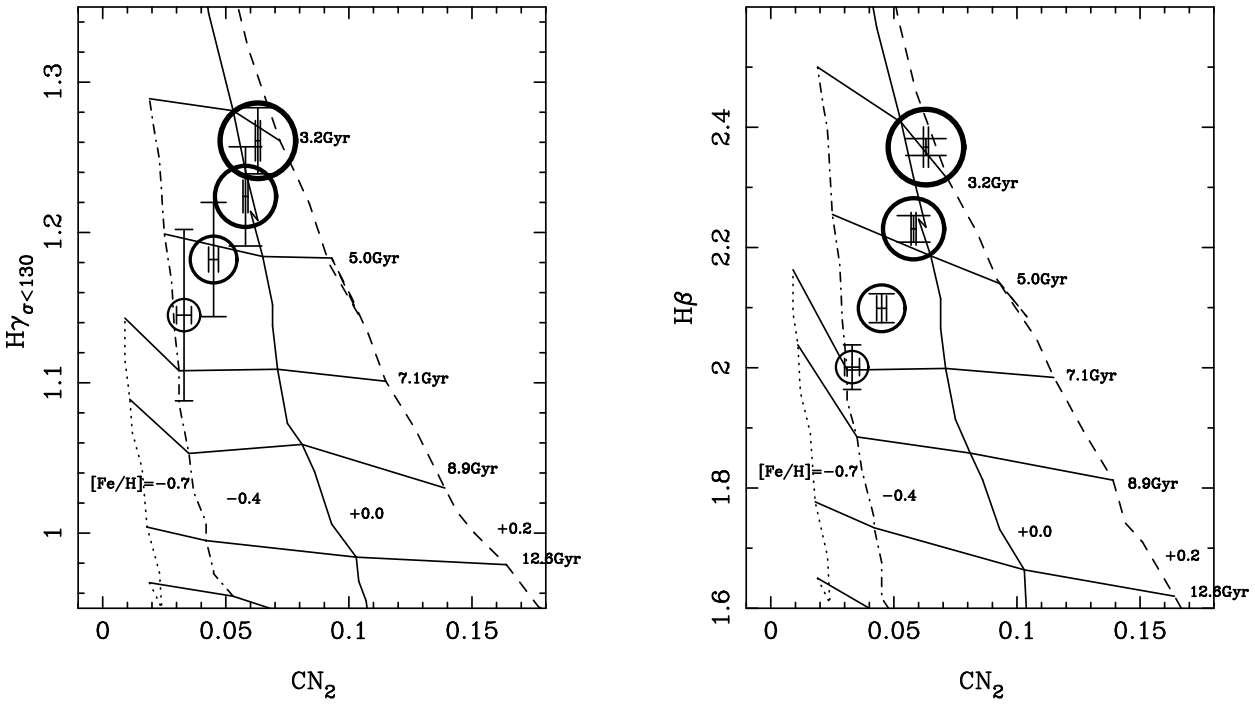

Fig. 5.— The M32 Hβ (right panel) and H$\gamma_{\sigma<130}$ (left panel) indices are plotted versus the CN_2 index for the Subaru data. Same symbols and models grid lines as for Fig. 1.

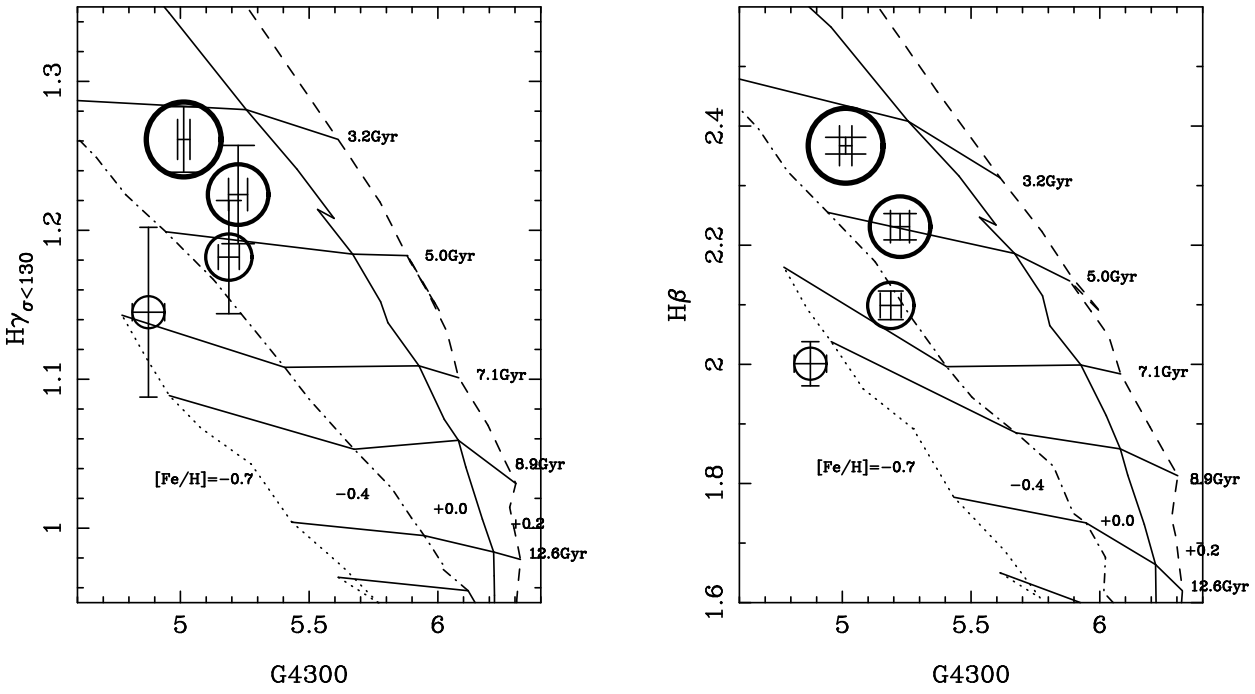

Fig. 6.— The M32 Hβ (right panel) and H$\gamma_{\sigma<130}$ (left panel) indices are plotted versus the G-band index for the Subaru data. Same symbols and models grid lines as for Fig. 1.

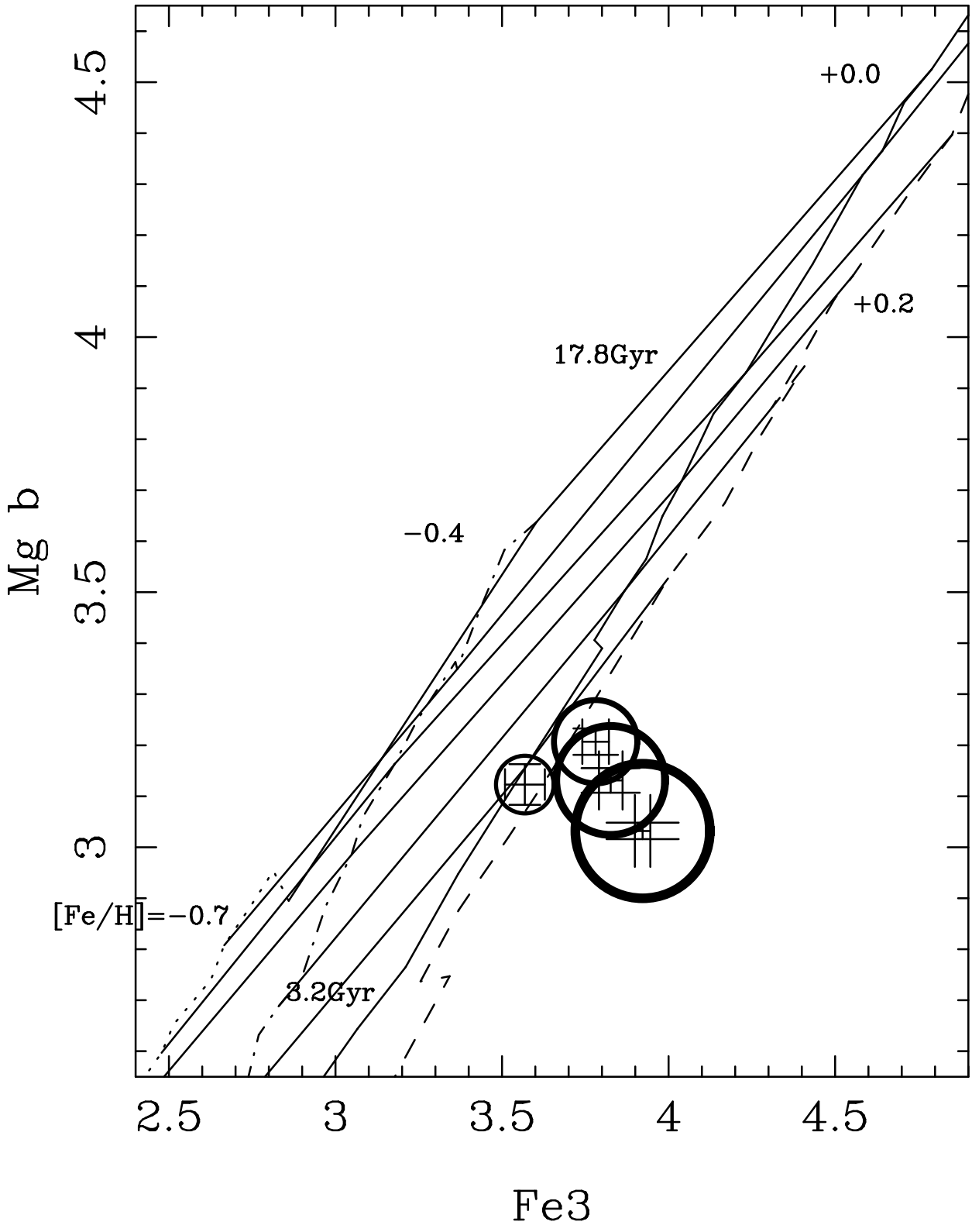

Fig. 7.— The M32 Mg b index is plotted versus the Fe3 index for the Subaru data. Same symbols and models grid lines as for Fig. 1.

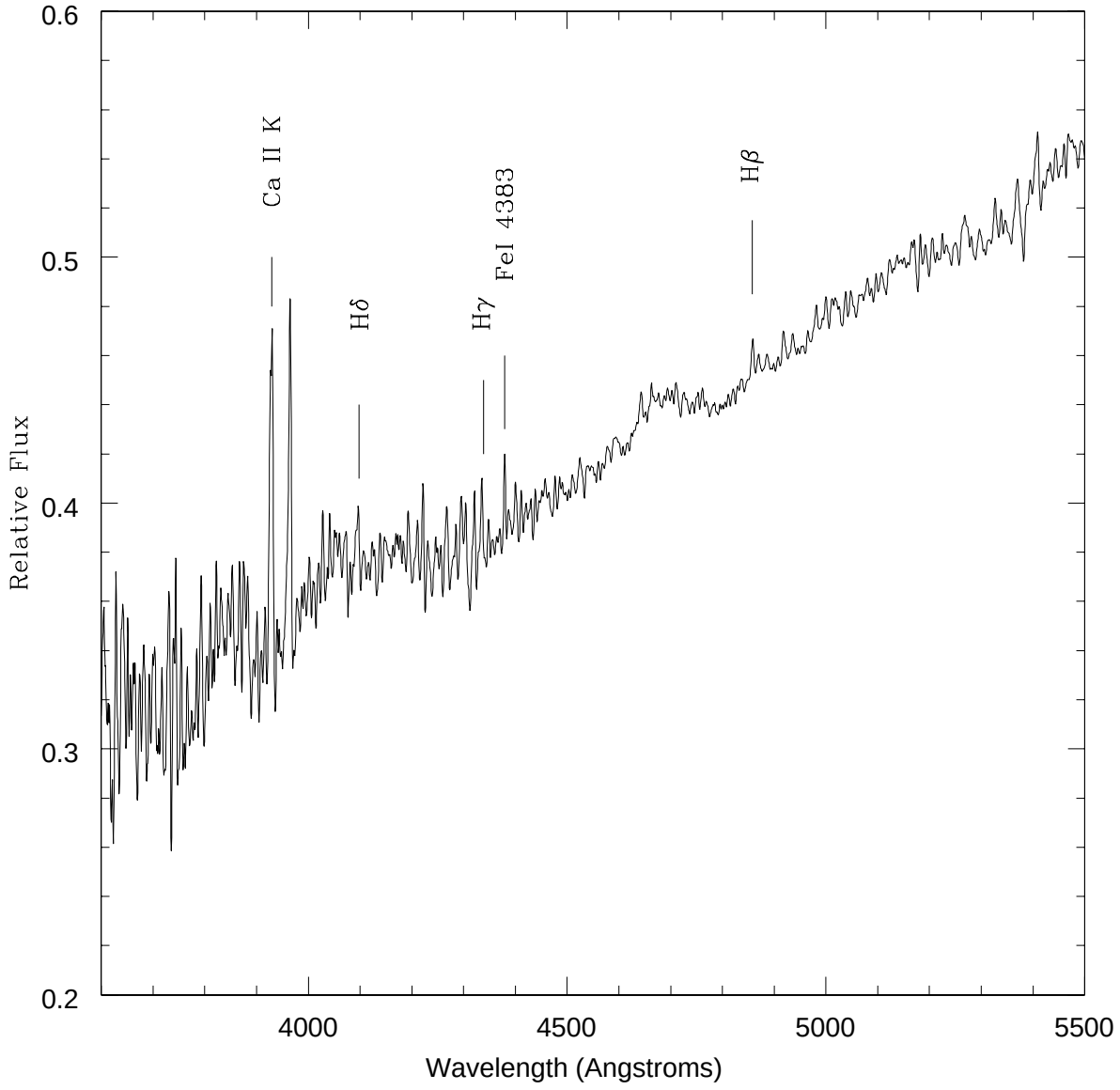

Fig. 8.— The spectrum at 30″ radius is divided by that in the nucelus for the FAST data. This ratio spectrum demonstrates that all principal spectral features, some of which are specifically marked, show up in emission, thus indicating that they are stronger in the nucleus of M32. Note that the large overall color gradient is probably an artifact of extracting the nuclear spectrum with a small aperture.

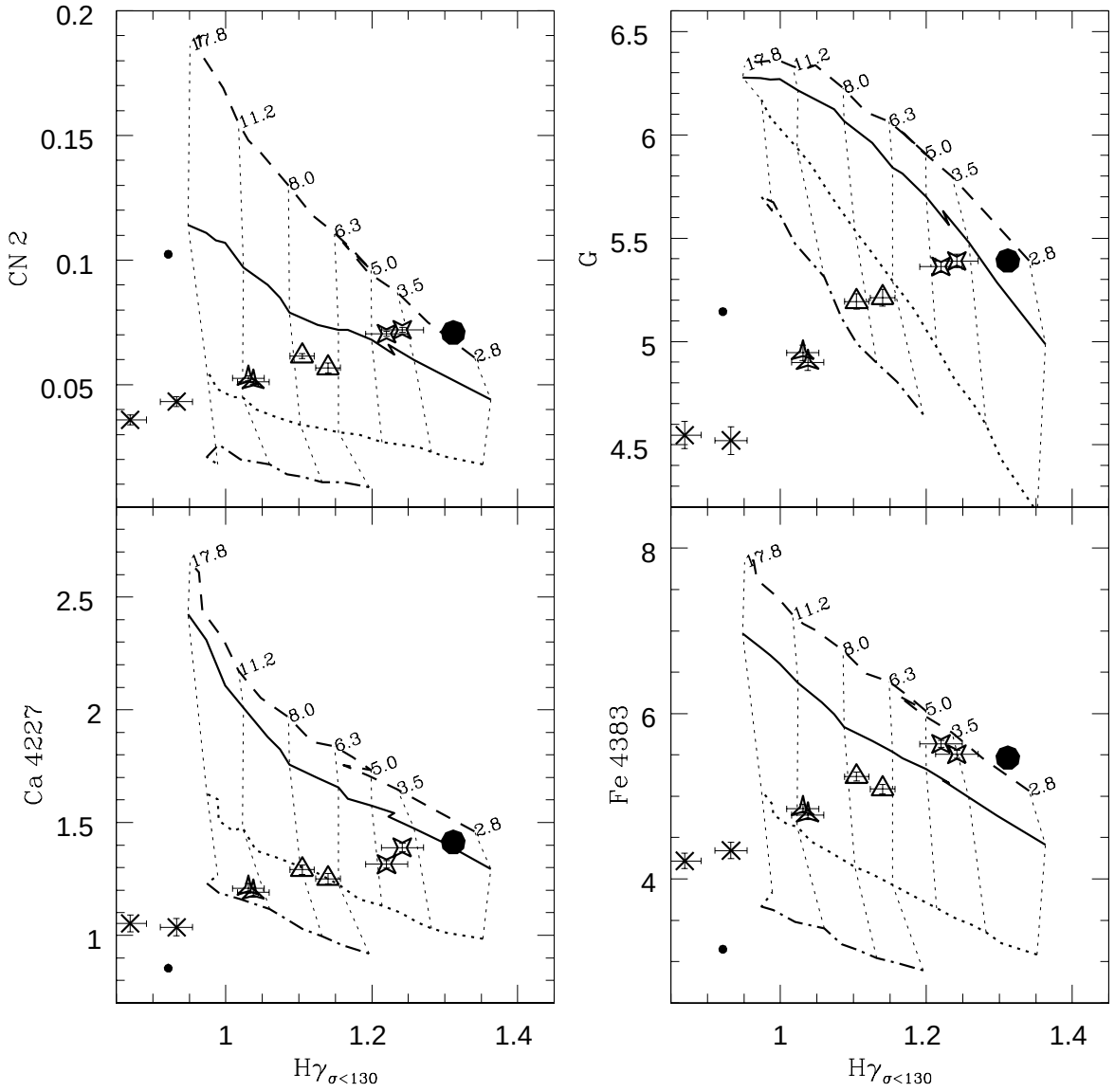

Fig. 9.— Various Lick spectral indices are plotted versus the H$\gamma_{\sigma<130}$ index for the Mayall telescope data for both M32 and for the Galactic globular cluster 47 Tuc. The small filled circle denotes 47 Tuc. The large filled circle represents data for the M32 nucleus. The pairs of starred squares, open triangles, starred triangles, and x's represent data at radial distances of 4.1″, 8.6″, 19.3″and 34.5″, respectively. Also plotted are model grid lines, with ages marked on the nearly vertical grid lines, ranging from 2.8 Gyr to 17.8 Gyr. Horizontal lines of constant metallicity are, from top to bottom, [Fe/H]=+0.2, 0.0, -0.4, and -0.7.

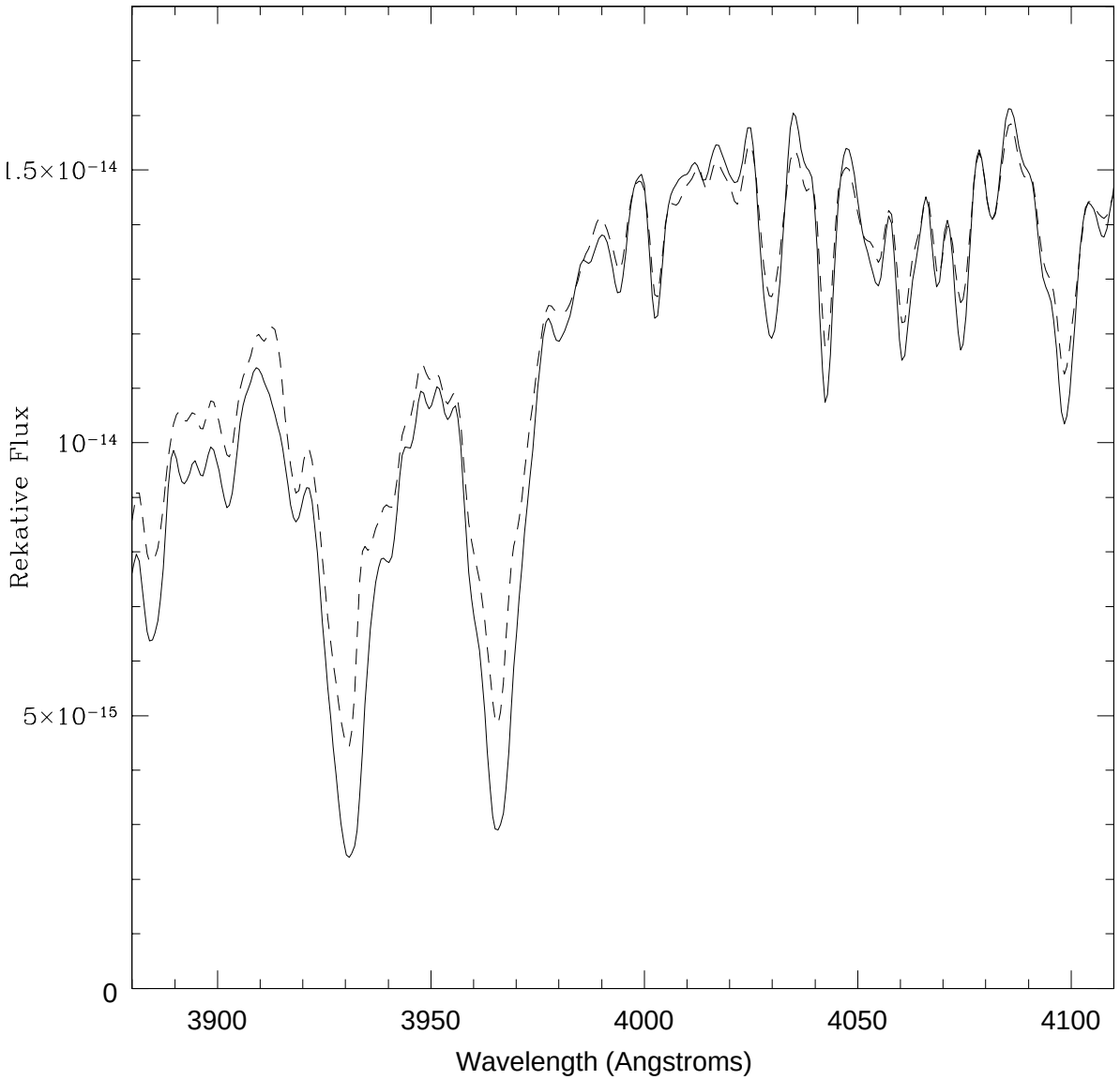

Fig. 10.— The nuclear spectrum of M32 (solid line) acquired with the Mayall telescope is overplotted with the spectrum at 30″ (dashed line). The spectrum at 30″ has been multiplied by a factor of 100. Note the shallower Ca II H and K lines in the spectrum at 30″, due to scattered light from the nucleus.

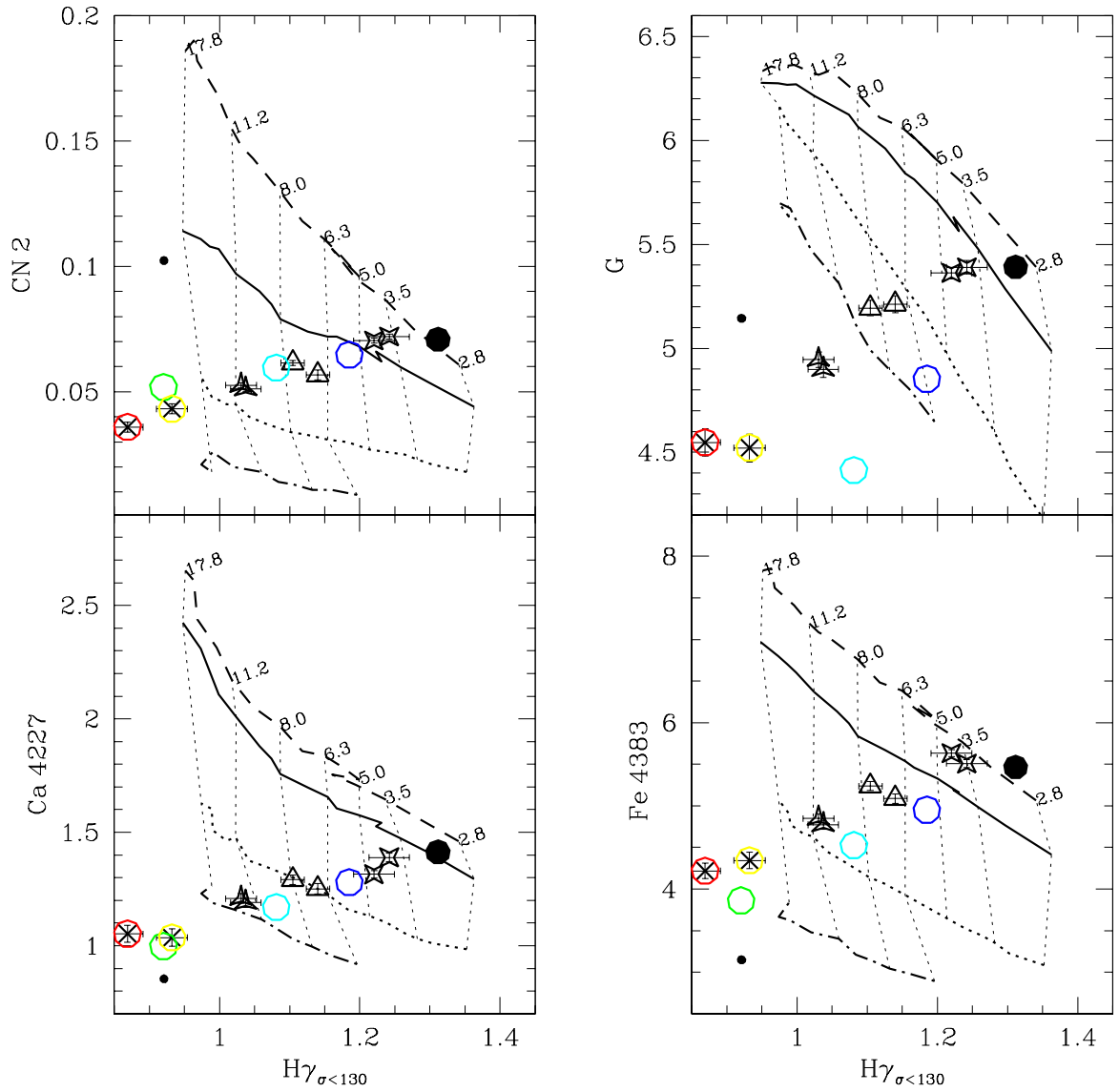

Fig. 11.— The same spectral index diagrams as in Fig. 9 are are replotted. As in Fig. 9, the symbols with error bars are the M32 data while 47 Tuc is represented by a small filled circle. All symbols and model grid lines are the same as in Fig. 9. In addition, we plot as large open circles the spectral indices obtained from adding varying amounts of a simulated featureless scattered light spectrum to the observed M32 nuclear spectrum. Bluer colored circles denote less scattered light component, while red indicates greater scattered light. This simple scattered light model appears to track the observed gradient in M32 indices.

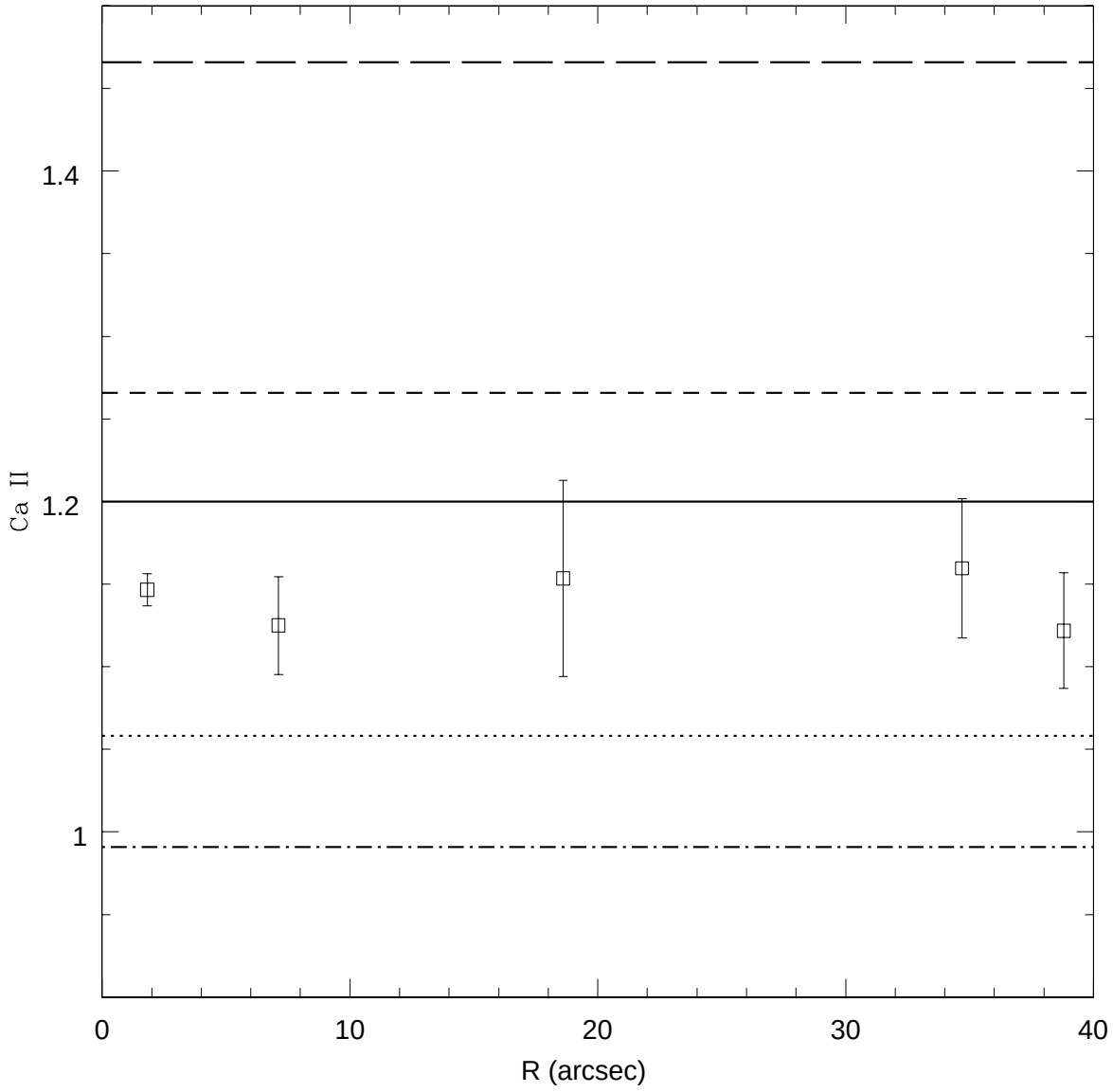

Fig. 12.— The Ca II index is plotted versus radial distance in M32 for the FAST data. The data are plotted as open squares with $\pm 1\sigma$ error bars. The solid line at at Ca II value of 1.2 shows the expected value for an entirely cool star population. The dotted and dot-dash lines represent the Ca II values found when the spectrum of an A4V star is added to that of M32 at the 5% and 10% levels respectively, with normalization at 4000 Å. The short and long dashed lines represent the values found when the A4V spectrum is subtracted off at 5% and 10% levels.

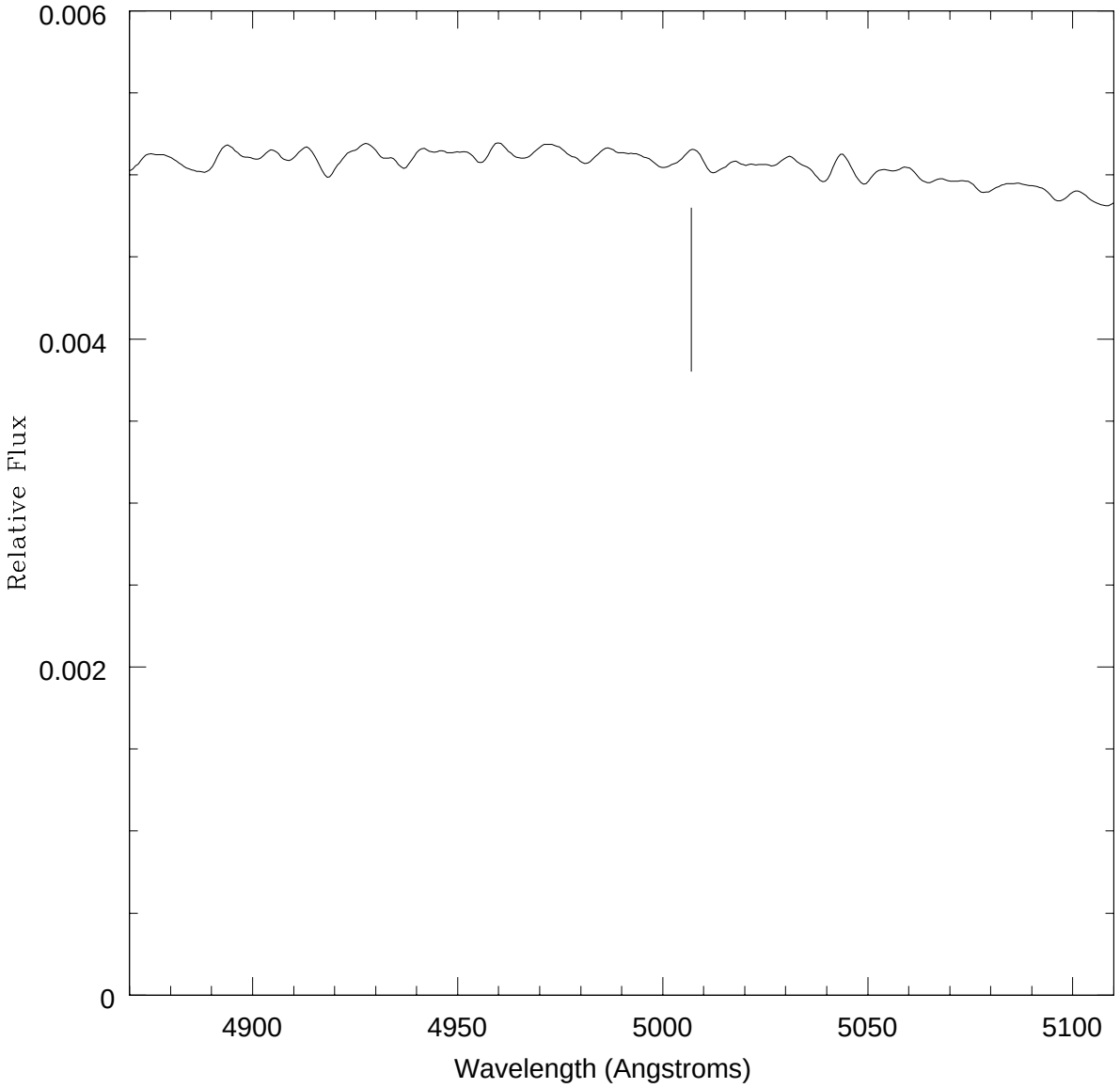

Fig. 13.— Ratio spectrum of the nucleus of M32 divided by the integrated spectrum of M67 is plotted in the region of the [OIII]λ5007 emission line. The expected location of [OIII]λ5007 emission is marked.

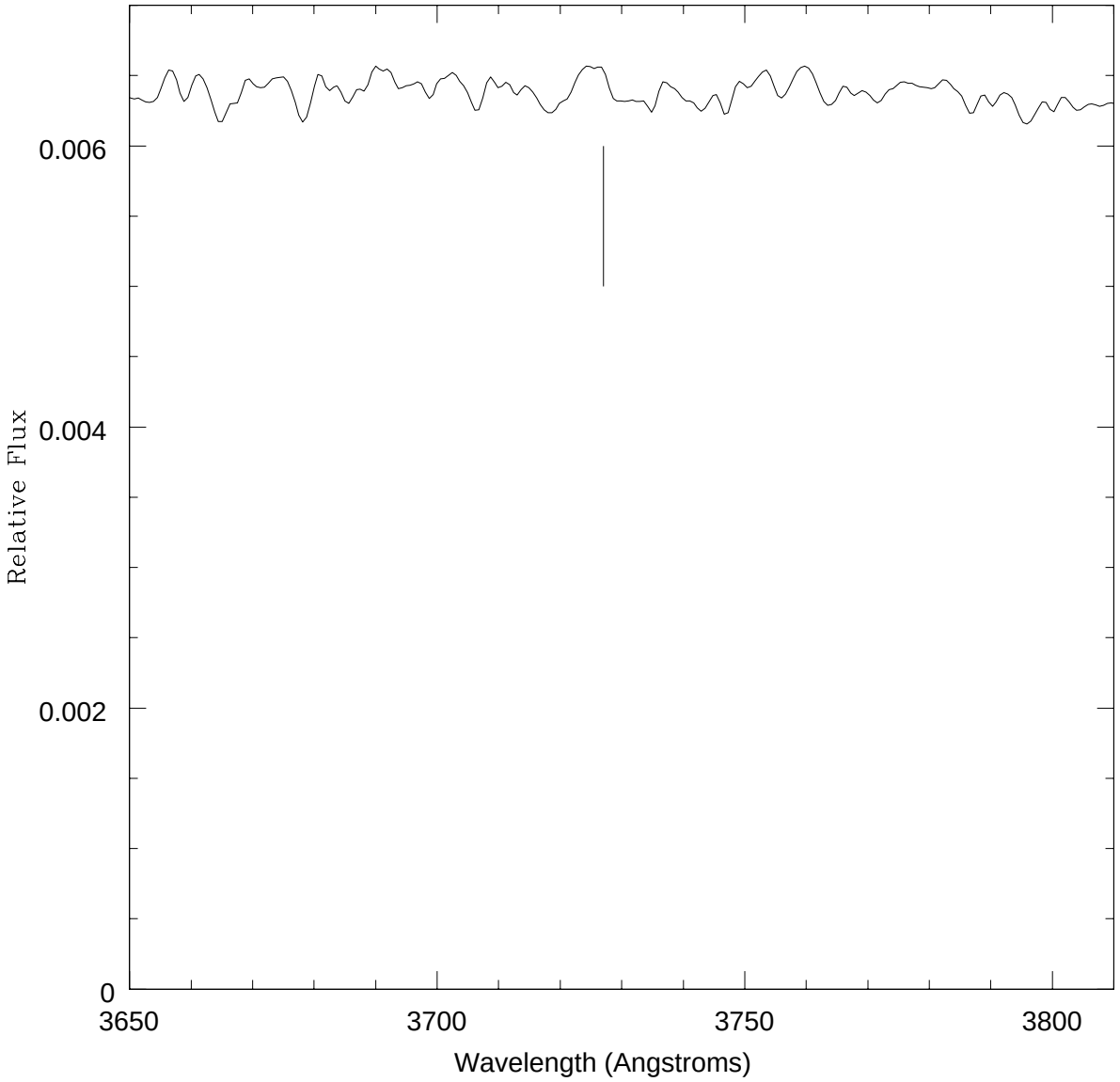

Fig. 14.— Ratio spectrum of the nucleus of M32 divided by the integrated spectrum of M67 is plotted in the region of the [OII]λ3727 emission line. The expected location of [OII]λ3727 emission is marked.

Table 1. Journal of Observations

UT Date	Telescope	Slit Position	PA	Exposure Time	Slit Width	Extraction Area	Wavelength Coverage	Resolutio FWHM
12/28/2000	Tillinghast + FAST	M32 Nucleus	90	8 x 240s	3″	±5.7″	3600 - 5500 Å	3.1 Å
12/28/2002	Tillinghast + FAST	M32 Offset 5″	-20	900s	3″	±9.1″	···	···
12/28/2002	Tillinghast + FAST	M32 Offset 15″	-20	2 x 900s	3″	±22.8″	···	···
12/28/2002	Tillinghast + FAST	Sky Offset 10′ S	-20	900s	3″	···	···	···
12/28/2002	Tillinghast + FAST	M32 Offset 30″	-20	7 x 900s	3″	±34.2″	···	···
···	···	···	···	···	···	±54.7	···	···
12/28/2002	Tillinghast + FAST	Sky Offset 10′ S	-20	4 x 900s	3″	···	···	···
01/28/2003	Subaru + FOCAS	M32 Nucleus	80	2 x 300s	0.6″	±3″	3960 - 5560 Å	3.1 Å
01/28/2003	Subaru + FOCAS	M32 Offset by 10″	80	3 x 900s	0.6″	··· [a]	···	···
01/28/2003	Subaru + FOCAS	M32 Sky Offset 6′ E	80	900s	0.6″	···	···	···
06/18/1996	Mayall + R-C Spectro	M32 Nucleus	102	1800s	2″	··· [b]	3300 - 4770 Å	3.1 Å
06/18/1996	Mayall + R-C Spectro	Sky Offset by	102	1800s	2″	···	···	···
06/19/1996	Mayall + R-C Spectro	M32 Nucleus	100	1800s	2″	··· [b]	···	···
06/19/1996	Mayall + R-C Spectro	Sky Offset by	100	1800s	2″	···	···	···
06/20/1996	Mayall + R-C Spectro	M32 Nucleus	155	2 x 1800s	2″	··· [b]	···	···
06/20/1996	Mayall + R-C Spectro	Sky Offset by	155	1800s	2″	···	···	···

[a]Extractions were made at 10−14″, 14.1−31.6″, 24.2−39.3″

[b]Extractions were made at 0−1.4″, 2.8−5.5″, 6.2−11.0″, 11.7−26.9″, 27.6−41.4″

Table 2. Spectral Indices and Errors for Subaru Data[a]

Radius ”	Radius R_e	$H\gamma_{\sigma<130}$ $\pm1\sigma$ $H\beta$ $\pm1\sigma$	$H\gamma_{125}$ $\pm1\sigma$ Fe5015 $\pm1\sigma$	$H\delta_A$ $\pm1\sigma$ Mg_1 $\pm1\sigma$	$H\gamma_A$ $\pm1\sigma$ Mg_2 $\pm1\sigma$	$H\delta_F$ $\pm1\sigma$ Mg b $\pm1\sigma$	$H\gamma_F$ $\pm1\sigma$ Fe5270 $\pm1\sigma$	CN1 $\pm1\sigma$ Fe5335 $\pm1\sigma$	CN2 $\pm1\sigma$ Fe5406 $\pm1\sigma$	Ca4226 $\pm1\sigma$ [MgFe] $\pm1\sigma$	G4300 $\pm1\sigma$ Fe3 $\pm1\sigma$	Fe4383 $\pm1\sigma$ Ca II $\pm1\sigma$
0.7	0.02	1.261	1.055	-1.178	-4.342	0.996	-0.629	0.023	0.063	1.242	5.013	5.364
		0.022	0.018	0.032	0.027	0.021	0.016	0.001	0.001	0.014	0.024	0.032
		2.367	5.859	0.046	0.159	3.032	3.271	3.131	2.021	3.115	3.922	···
		0.014	0.031	0.000	0.000	0.016	0.017	0.020	0.015	0.007	0.014	···
10.3	0.29	1.224	1.045	-1.324	-4.421	0.846	-0.757	0.019	0.058	1.348	5.224	5.168
		0.033	0.028	0.051	0.041	0.033	0.026	0.001	0.001	0.022	0.037	0.050
		2.231	5.696	0.046	0.161	3.131	3.241	3.070	1.953	3.143	3.826	···
		0.022	0.047	0.001	0.001	0.024	0.026	0.030	0.023	0.011	0.021	···
20.8	0.59	1.182	1.026	-1.126	-4.413	0.766	-0.822	0.008	0.045	1.256	5.188	5.107
		0.038	0.031	0.057	0.046	0.038	0.029	0.001	0.002	0.025	0.041	0.056
		2.099	5.677	0.046	0.162	3.207	3.192	3.044	1.957	3.162	3.781	···
		0.024	0.053	0.001	0.001	0.026	0.029	0.034	0.026	0.012	0.024	···
30.3	0.86	1.145	0.947	-1.186	-4.265	0.488	-0.869	-0.004	0.033	1.177	4.876	4.733
		0.057	0.047	0.086	0.070	0.058	0.044	0.002	0.003	0.038	0.063	0.085
		2.001	5.486	0.043	0.158	3.123	3.042	2.931	1.933	3.054	3.569	···
		0.037	0.080	0.001	0.001	0.040	0.044	0.051	0.039	0.019	0.036	···

[a]All spectral indices have been determined after first smoothing the spectra to a final effective velocity dispersion of 130 km s^{-1} , when compared to a template with intrinsic spectral resolution of 1.8 Å FWHM. This corresponds to a final spectral resolution of 4.75 Å FWHM at 4300 Å. Note that our spectral resolution is not that of the Lick/IDS system resolution. As well, the indices are measured from the flux calibrated spectra, i.e., not the Lick/IDS instrumental profile.

Table 3. Spectral Indices and Errors for Tillinghast Data[a]

Radius ”	Radius R_e	$H\gamma_{\sigma<130}$ $\pm1\sigma$ $H\beta$ $\pm1\sigma$	$H\gamma_{125}$ $\pm1\sigma$ Fe5015 $\pm1\sigma$	$H\delta_A$ $\pm1\sigma$ Mg_1 $\pm1\sigma$	$H\gamma_A$ $\pm1\sigma$ Mg_2 $\pm1\sigma$	$H\delta_F$ $\pm1\sigma$ Mg b $\pm1\sigma$	$H\gamma_F$ $\pm1\sigma$ Fe5270 $\pm1\sigma$	CN1 $\pm1\sigma$ Fe5335 $\pm1\sigma$	CN2 $\pm1\sigma$ Fe5406 $\pm1\sigma$	Ca4226 $\pm1\sigma$ [MgFe] $\pm1\sigma$	G4300 $\pm1\sigma$ Fe3 $\pm1\sigma$	Fe4383 $\pm1\sigma$ Ca II $\pm1\sigma$
2.1	0.06	1.266	1.110	-1.097	-4.472	0.984	-0.712	0.031	0.073	1.395	5.438	5.458
		0.014	0.011	0.068	0.068	0.073	0.033	0.002	0.003	0.051	0.051	0.110
		2.330	5.815	0.092	0.211	3.066	3.208	3.0 03	2.002	3.086	3.890	1.147
		0.063	0.101	0.001	0.002	0.034	0.051	0.0 56	0.034	0.018	0.045	0.010
7.1	0.24	1.214	1.060	-0.998	-4.283	0.923	-0.575	0.039	0.082	1.424	5.308	5.529
		0.071	0.058	0.101	0.085	0.067	0.054	0.003	0.003	0.045	0.076	0.105
		2.274	5.617	0.081	0.194	3.083	3.300	2.959	1.896	3.107	3.930	1.125
		0.043	0.091	0.001	0.001	0.044	0.048	0.054	0.040	0.019	0.042	0.030
18.6	0.64	1.103	0.955	-0.876	-3.969	0.964	-0.640	0.038	0.085	1.286	5.466	4.811
		0.060	0.050	0.086	0.073	0.057	0.046	0.002	0.003	0.038	0.065	0.089
		2.234	5.449	0.081	0.199	3.213	3.057	2.758	1.900	3.057	3.542	1.154
		0.038	0.080	0.001	0.001	0.038	0.041	0.047	0.035	0.018	0.036	0.059
34.7	1.19	1.011	0.889	-1.151	-4.152	0.795	-0.731	0.029	0.071	1.422	5.429	5.088
		0.043	0.036	0.059	0.052	0.040	0.033	0.002	0.002	0.027	0.047	0.065
		2.150	5.082	0.078	0.195	3.112	3.059	2.818	1.349	3.024	3.655	1.160
		0.027	0.058	0.001	0.001	0.028	0.029	0.031	0.023	0.012	0.026	0.042
38.8	1.33	1.136	1.021	-0.833	-4.143	0.718	-0.732	0.020	0.059	1.337	5.266	4.872
		0.048	0.040	0.067	0.059	0.045	0.037	0.002	0.002	0.031	0.052	0.072
		2.099	4.955	0.075	0.191	3.067	2.961	2.585	1.337	2.916	3.473	1.122
		0.030	0.065	0.001	0.001	0.031	0.033	0.037	0.026	0.014	0.029	0.035

[a]All spectral indices have been determined after first smoothin g the spectra to a final effective velocity dispersion of 130 km s^{-1} , when compared to a template with intrinsic spectral resolution of 1.8 Å FWHM. This corresponds to a final spectral resolution of 4.75 Å FWHM at 4300 Å. Note that our spectral resolution is not that of the Lick/IDS system resolution. As well, the indices are measured from the flux calibrated spectra, i.e., not the Lick/IDS instrumental profile.